



A physically-based formulation for texture evolution during dynamic recrystallization. A case study for ice

Thomas Chauve, Maurine Montagnat, Véronique Dansereau, Pierre Saramito, Kévin Fourteau, Andrea Tommasi

► To cite this version:

Thomas Chauve, Maurine Montagnat, Véronique Dansereau, Pierre Saramito, Kévin Fourteau, et al.. A physically-based formulation for texture evolution during dynamic recrystallization. A case study for ice. Article soumis, inPress. hal-04231338v1

HAL Id: hal-04231338

<https://hal.science/hal-04231338v1>

Submitted on 6 Oct 2023 (v1), last revised 4 Mar 2024 (v3)

HAL is a multi-disciplinary open access archive for the deposit and dissemination of scientific research documents, whether they are published or not. The documents may come from teaching and research institutions in France or abroad, or from public or private research centers.

L'archive ouverte pluridisciplinaire **HAL**, est destinée au dépôt et à la diffusion de documents scientifiques de niveau recherche, publiés ou non, émanant des établissements d'enseignement et de recherche français ou étrangers, des laboratoires publics ou privés.



Distributed under a Creative Commons Attribution 4.0 International License



A physically-based formulation for texture evolution during dynamic recrystallization. A case study for ice.

Thomas Chauve^{*, a}, Maurine Montagnat^{a, b}, Véronique Dansereau^c,
Pierre Saramito^d, Kévin Fourteau^b and Andréa Tommasi^e

^a Univ. Grenoble Alpes, CNRS, IRD, G-INP, IGE, Grenoble, France

^b Univ. Grenoble Alpes, Université de Toulouse, Météo-France, CNRS, CNRM, Centre d'Études de la Neige, Grenoble, France

^c Institut des Sciences de la Terre, Université Grenoble Alpes, CNRS (5275), Grenoble, France

^d Lab. Jean Kuntzmann – CNRS, Université Grenoble-Alpes, F-38041 Grenoble, France

^e Géosciences Montpellier - CNRS, Université de Montpellier, France

E-mail: thomas.chauve@univ-grenoble-alpes.fr (T. Chauve)

Abstract. Dynamic recrystallization can have a strong impact on texture development during the deformation of polycrystalline materials at high temperature, in particular for those with strong viscoplastic anisotropy such as ice. Owing to this anisotropy, recrystallization is essential for ensuring strain compatibility. The development of recrystallization textures leads to significant mechanical softening. Accurately predicting ice texture evolution due to recrystallization during tertiary creep remains a challenge, yet is crucial to account adequately for texture-induced anisotropy in large-scale models of glacial ice flow.

We propose a new formulation for texture evolution due to dynamic recrystallization. This formulation is physically-based on an orientation attractor which maximizes the Resolved Shear Stress on the easiest slip system in the crystal. The attractor is implemented in an equation of evolution of the crystal orientation with deformation, which is coupled to an anisotropic viscoplastic law that provides the mechanical response of the ice crystal. The set of equations, which is the core of the *R³iCe* open source model is solved using Finite Elements Method with a semi implicit scheme coded using the Rheolef library. *R³iCe* is validated by comparison with laboratory creep data for ice polycrystals under simple shear, uniaxial compression and tension. It correctly reproduces the texture evolution and the mechanical softening observed during tertiary creep. *R³iCe* therefore allows predicting enhancement factors that may be implemented in large-scale flow models. Although the validation was performed for ice, the *R³iCe* implementation is generic and applies for any material adequately described using a anisotropic law.

Keywords. dynamic recrystallization, texture, viscoplastic anisotropy, finite elements method, ice.

This article is a draft (not yet accepted!)

a	Scalar		
\mathbf{a}	Vector		
\mathbf{A}	Tensor		
\mathbf{A}^D	Deviatoric part of \mathbf{A}	$\mathbf{A}^D = \mathbf{A} - \frac{1}{\dim(\mathbf{A})} \text{Tr}(\mathbf{A})$	$A_{ij}^D = A_{ij} - \frac{\delta_{ij}}{\dim(\mathbf{A})} \text{Tr}(\mathbf{A})$
\otimes	Tensorial (dyadic) product	$\mathbf{A} = \mathbf{b} \otimes \mathbf{c}$	$A_{ij} = b_i c_j$
$\text{Tr}()$	Trace of a tensor	$\text{Tr}(\mathbf{A})$	A_{ii}
$\dim()$	dimension of a tensor	$\dim(\mathbf{A})$	
∇	∇ operator	$\left(\frac{\partial}{\partial x}, \frac{\partial}{\partial y}, \frac{\partial}{\partial z} \right)$	$\frac{\partial}{\partial x_i}$
\cdot	Scalar product	$\mathbf{a} \cdot \mathbf{b}$	$a_i b_i$
$:$	Double contracted product	$\mathbf{A} : \mathbf{B}$	$A_{ij} B_{ij}$

Table 1. Mathematical notations

Notation

1. Introduction

Dynamic recrystallization (DRX) is a mechanism by which local stress incompatibilities and local strain heterogeneities are relaxed. By *local*, we mean the scale of the grains that constitute crystalline materials such as ice, metals or most rocks [1]. Dynamic recrystallization occurs in plastically deforming materials at high temperature. It is characterized by the nucleation of new grains and grain boundary migration and can lead to the complete re-organisation of the microstructure, i.e., the grain shape and size, and to a drastic modification of the texture, i.e., the crystallographic orientations of grains [2–6]. These changes in the microstructure and texture may lead to modification of the rheological behavior, that is, the response of the material to imposed stresses or strains.

Ice is a hexagonal crystalline material (figure 1) that deforms, on Earth, at a temperature very close to its melting point. In the ductile regime, its deformation is controlled by a strong viscoplastic anisotropy, with dislocations gliding almost solely on the basal plane [7, 8]. The orientation of an ice crystal therefore has a strong control on its viscosity. Consequently, the distribution of crystallographic orientations in polycrystalline ice impacts the mechanical response in the form of a texture-induced viscoplastic anisotropy [9].

Microstructural evidence for recrystallization is systematically observed along deep ice cores, where it is supposed to contribute variably to the measured texture, depending on the deformation conditions (temperature, impurities). To interpret the texture evolution along ice cores, a model has been proposed by De la Chapelle et al. 1998 [10]. This model states that DRX may either slow down the strain-induced texture evolution (the so-called "continuous" dynamic recrystallization regime) or drastically modify the texture, with the final texture controlled by the stress state (the "discontinuous" dynamic recrystallization regime). Whether both DRX regimes are more or less active depends on the temperature and strain conditions along the ice core [11, 12]. In deep section of ice sheet, along ice streams, and in glacier areas where temperature and strain are high, DRX leads to highly anisotropic textures, in particular when simple shear is dominant (see e.g. [13–16]). These textures result in strong viscoplastic anisotropy, which can either enhance strain rates or slow down the deformation. For instance, the vertical cluster of *c*-axes observed along ice cores will produce acceleration of horizontal shearing but slows down compres-

* Corresponding author.

sion [17–22]. To model the deformation of an ice sheet, it is therefore essential to consider the effect of DRX on the texture evolution.

Dynamic recrystallization in ice has been extensively studied in the laboratory. The studies allowed to characterize the basic mechanisms at play, nucleation and grain-boundary migration, and the impact of strain heterogeneities on their kinetics (see e.g. [23–31]). [2] was a pioneer in performing a large number of experiments in simple shear and compression to characterize the effect of DRX on texture evolution and macroscopic mechanical behavior. He proposed that the creep rate accelerations characteristic of the tertiary creep stage could result from the development of DRX textures favorable to the activation of basal slip. This study is likely at the origin of the widely established belief that DRX favors "well-oriented" grains relative to the imposed stress. Since then, work by Grennerat et al. 2012 [32] revealed that the strain field during deformation in polycrystalline ice is highly heterogeneous, with no simple relation between intensity of the local strain and the Schmid factor, a parameter that quantifies the orientation relation between a crystal and the imposed macroscopic stress. More recently, direct measures of the evolution of the strain field with DRX by Chauve et al. 2017 [33] have further illustrated the heterogeneity of the mechanical behavior at the grain scale and its impact on DRX. They showed that DRX tends to homogenize the strain field in relation with local microstructure changes.

Altogether these data show that although resulting from a complex interplay between the imposed stress and strain states, the local microstructure and the resulting redistribution of stresses, the experimentally-measured DRX textures favor macroscopic flow, what is reflected by a marked strain softening at the onset of tertiary creep [21, 24, 26]. Further texture evolution during tertiary creep results in a quasi constant strain-rate for bulk strain higher than about 10%; this "stationary" strain rate is independent on the initial texture and is controlled by the imposed stress [34–37]. This contrasts with the minimum strain rate observed at the onset of secondary creep, which depends on the initial texture. At secondary creep, the classical Glen's law relates the strain rate to the applied stress non-linearly (through an exponent of 3 and an Arrhenius type of dependence to the temperature) [8, 38]. This law does not hold in tertiary creep but it has been adapted by modifying the stress exponent to a value slightly higher than 3 and adding a strain-rate enhancement factor (the ratio between the strain rate measured at tertiary creep and the minimum strain rate at secondary creep). This enhancement factor, of between 4 in compression and 8 in simple shear [21, 37] accounts for the impact of the DRX texture on the strain softening at tertiary creep.

Textures that develop during DRX in ice are well constrained. Under uniaxial compression, the textures measured at tertiary creep are characterized by the **c**-axes being oriented within a girdle characterized by a cone angle between 30° and 50° from the compression axis depending on the conditions (temperature T , stress). These textures are stable, that is evolve very slowly at strains higher than 10% [2, 23, 26, 28, 30, 37, 39]. During simple shear, tertiary creep textures seem to evolve with increasing strain from a two-maxima pattern, that is symmetric relative to the extension direction, toward a strongly clustered texture, with **c**-axes aligned in a direction perpendicular to the shear plane [24, 25, 31, 40, 41].

Although strain-induced texture development in ice has been successfully simulated using various approaches of various complexity [17, 18, 42, 43], these approaches fail to reproduce the tertiary creep experimental textures and the rare models simulating the effect of dynamic recrystallization are rather unsatisfactory, either in terms of texture patterns or in terms of kinetics of texture evolution [44–48]. The discrepancies between models and observations results from the use of a simplified, mean-field approach that does not enable DRX mechanisms to be properly represented [44, 45], or from limitations in the deformation modeling frame despite considering a high complexity in the microstructure evolution [46]. In the case of Richard et al.

2021 [47] and Rathmann et al. 2021 [48], the simulated textures are very close to the observed ones, but the kinetics of evolution is not. This discrepancy may result from the use of a Sachs approximation for modeling the mechanical response of the polycrystal (or similar in the case of [47]). This hypothesis was shown by Castelnau et al. 1996 [49] to result into a too soft mechanical response and incoherency in the grain rotation calculation.

In the present work, we propose a new formulation to predict the impact of dynamic recrystallization on the texture evolution of polycrystalline materials, like ice. This formulation couples the Continuous Transverse Isotropic (CTI) law, which represents the anisotropic response of the ice crystal, to a crystal orientation evolution equation that accounts for DRX. The contribution of DRX is modeled by a physically-based orientation attractor that maximizes the Resolved Shear Stress on the easiest slip system in the crystal (basal slip for ice). This set of equations, named *CTI-RX*, is solved in a full-field model using Finite Element Methods (FEM).

In section 2 we present the *CTI-RX* model: its equations for the CTI law (section 2.1) and the proposed formulation for the evolution of the *c*-axis (section 2.2). The numerical scheme designed to solve these equations is described in section 3. Section 4 presents the calibration and the validation for a case without dynamic recrystallization. Section 5 evaluates the capability of the model to reproduce the evolution of the texture and the mechanical response by comparing with experimental data for tertiary creep of ice polycrystals subjected to axial compression, axial extension and simple shear.

2. *CTI-RX*- a model for the ice single crystal behavior

2.1. *The Continuous Transverse Isotropic behavior*

Following [50–54], we account for the viscoplastic anisotropy of the ice single crystal by modelling its mechanical behavior using the Continuous Transverse Isotropic (CTI) law. In the framework, the viscoplastic response of the ice single crystal depends on the orientation of the *c*-axis and is isotropic in the basal plane (see Figure 1). It builds on the theoretical work of Boehler [55] 1987, which has shown, through geometrical arguments, that the relation between the deviatoric stress *S* and the deviatoric strain rate *D* in a transverse isotrope symmetry derives from a potential ϕ_S that is built out of a combination of the following four invariants:

$$\mathcal{B}_{CTI} = [Tr(\mathbf{S}^2), Tr(\mathbf{S}^3), Tr(\mathbf{MS}), Tr(\mathbf{MS}^2)], \quad (1)$$

with $\mathbf{M} = \mathbf{e}_3 \otimes \mathbf{e}_3$ where \mathbf{e}_3 is the direction of the isotropy plane (figure 1). Within this framework, the constitutive equation relating the deviatoric strain rate to the deviatoric stress is given by:

$$\mathbf{D} = \left(\frac{\partial \phi_S}{\partial \mathbf{S}} \right)^D \quad (2)$$

where ϕ_S is a potential expressed on the \mathcal{B}_{CTI} base. This potential is described below in the linear ($\phi_S^{(1)}$) and non linear ($\phi_S^{(n)}$) cases.

2.1.1. *The linear CTI formulation*

To obtain a linear CTI formulation, the potential, $\phi_S^{(1)}$, must be quadratic. It is therefore constructed from the quadratic invariants taken from the \mathcal{B}_{CTI} base as:

$$\phi_S^{(1)} = \delta_1 Tr(\mathbf{S}^2) + \delta_2 Tr(\mathbf{MS})^2 + \delta_3 Tr(\mathbf{MS}^2). \quad (3)$$

Considering the following derivation rules,

$$\frac{\partial Tr(\mathbf{MS})}{\partial \mathbf{S}} = \mathbf{M}, \quad \frac{\partial Tr(\mathbf{S}^2)}{\partial \mathbf{S}} = 2\mathbf{S}, \quad \frac{\partial Tr(\mathbf{MS}^2)}{\partial \mathbf{S}} = \mathbf{MS} + \mathbf{SM}, \quad (4)$$

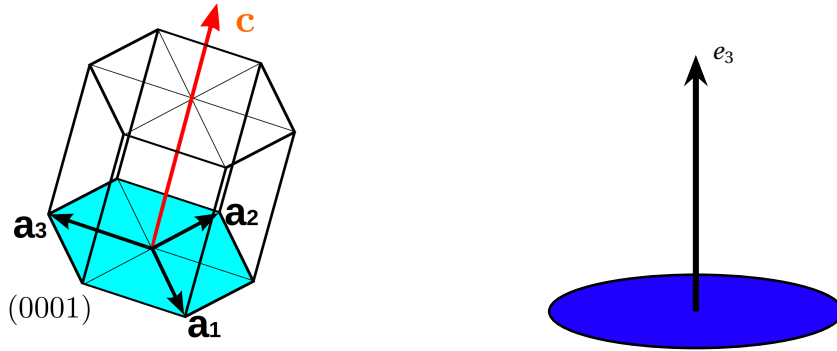


Figure 1. The transverse isotropic geometry is fully described by one direction, e_3 , that defines the plane of isotropy. For an ice single crystal, this direction corresponds to that of the c -axis (i.e. the normal to the basal (0001) plane).

the constitutive relation is given by

$$\mathbf{D} = \left(\frac{\partial \phi_S^{(1)}}{\partial \mathbf{S}} \right)^D = 2\delta_1 \mathbf{S} + 2\delta_2 \mathbf{M}^D \text{Tr}(\mathbf{M}\mathbf{S}) + \delta_3 (\mathbf{M}\mathbf{S} + \mathbf{S}\mathbf{M})^D. \quad (5)$$

In equation (5), the three independent parameters δ_i can be fitted from experimental data as detailed below.

In the present implementation of the model, the anisotropy of the ice single crystal (or grain) behavior is described using the following parameters:

- ψ_1 is the fluidity of the ice in shear, parallel to the basal plane, such that:

$${}^g D_{13} = \frac{\psi_1}{2} {}^g S_{13}, \quad {}^g D_{23} = \frac{\psi_1}{2} {}^g S_{23},$$

- β is the ratio between the fluidity in shear parallel to the basal plane and the one for shear within the basal plane, such that:

$${}^g D_{12} = \beta \frac{\psi_1}{2} {}^g S_{12},$$

where ${}^g \mathbf{X}$ defined the tensor in the single crystal reference frame.

- γ is the ratio between the viscosity in compression (or traction) along the \mathbf{c} -axis η_c and compression (or traction) in one direction ${}^g e_r$ within the basal plane, such that:

$${}^g S_{33} = 2\eta_c {}^g D_{33}, \quad \gamma {}^g S_{rr} = 2\eta_c {}^g D_{rr}$$

For sollicitations of similar amplitude in different directions, for instance along \mathbf{e}_3 or perpendicular to \mathbf{e}_3 (i.e. along \mathbf{e}_{rr}) $S = {}^g S_{33} = {}^g S_{rr}$, the strain rates are related by:

$${}^g D_{rr} = \gamma {}^g D_{33}$$

Using the above constraints on this single crystal behavior, identification gives (see appendix A for details):

$$\delta_1 = \frac{\psi_1 \beta}{4}, \quad \delta_2 = \frac{\psi_1}{2} \left(\beta \frac{\gamma + 2}{4\gamma - 1} - 1 \right), \quad \delta_3 = \frac{\psi_1}{2} (1 - \beta) \quad (6)$$

The constitutive equation (5) can also be expressed in an inverse manner as

$$\mathbf{S} = 2\alpha_1 \mathbf{D} + 2\alpha_2 \mathbf{M}^D \text{Tr}(\mathbf{M}\mathbf{D}) + \alpha_3 (\mathbf{M}\mathbf{D} + \mathbf{D}\mathbf{M})^D \quad (7)$$

with : $\alpha_1 = \frac{\eta_1}{\beta}$, $\alpha_2 = 2\eta_1 \left(\frac{\gamma}{\beta} - 1 \right)$, $\alpha_3 = 2\eta_1 \left(1 - \frac{1}{\beta} \right)$ and $\eta_1 = \frac{1}{\psi_1}$ and in terms of the potential

$$\phi_D^{(1)} = \alpha_1 \text{Tr}(\mathbf{D}^2) + \alpha_2 \text{Tr}(\mathbf{MD})^2 + \alpha_3 \text{Tr}(\mathbf{MD}^2) \quad (8)$$

(see [18] and appendix A for details).

2.1.2. The non-linear CTI formulation

A non-linear potential $\phi_D^{(n)}$ linking \mathbf{S} to $\mathbf{D}^{\frac{1}{n}}$ is obtained by taking the linear potential $\tilde{\phi}_D^{(1)} = \frac{1}{2\eta_1} \phi_D^{(1)}$ to a higher order, k :

$$\phi_D^{(n)} = A_n \left(\tilde{\phi}_D^{(1)} \right)^k. \quad (9)$$

Using the chain rule for deriving $\phi_D^{(n)}$ gives:

$$\mathbf{S} = \frac{\partial \phi_D^{(n)}}{\partial \mathbf{D}} = A_n k \left(\tilde{\phi}_D^{(1)} \right)^{k-1} \frac{\partial \tilde{\phi}_D^{(1)}}{\partial \mathbf{D}} \quad (10)$$

k is further obtained by identification of the power exponent on equation (10) in order to have $\mathbf{S} \sim \mathbf{D}^{\frac{1}{n}}$:

$$2(k-1) + 2 = \frac{1}{n} \implies k = \frac{n+1}{2n} \quad (11)$$

Therefore, a non-linear CTI law can be written:

$$\phi_D^{(n)} = \frac{4n}{n+1} \left(\alpha_1 \text{tr}(\mathbf{D}^2) + \alpha_2 \text{tr}(\mathbf{MD})^2 + \alpha_3 \text{tr}(\mathbf{MD}^2) \right)^{\frac{n+1}{2n}}, \quad (12)$$

leading to the following constitutive equation:

$$\mathbf{S} = \eta_n^* (2\alpha_1 \mathbf{D} + 2\alpha_2 \mathbf{M}^D \text{Tr}(\mathbf{MD}) + \alpha_3 (\mathbf{MD} + \mathbf{DM})^D), \quad (13)$$

with the effective viscosity

$$\eta_n^* = 2\eta_n \left(\alpha_1 \text{tr}(\mathbf{D}^2) + \alpha_2 \text{tr}(\mathbf{MD})^2 + \alpha_3 \text{tr}(\mathbf{MD}^2) \right)^{\frac{1-n}{2n}} \quad (14)$$

and α_i parameters:

$$\alpha_1 = \frac{1}{2\beta}, \quad \alpha_2 = \left(\frac{\gamma}{\beta} - 1 \right), \quad \alpha_3 = \left(1 - \frac{1}{\beta} \right). \quad (15)$$

It is worth noting that β links D_{12} to S_{12} through:

$$D_{12} = \frac{\psi_n}{2} \beta^{\frac{n+1}{2}} S_{12}^n. \quad (16)$$

Therefore, β depends on the non-linearity, i.e. on the value of n . A similar enhancement will be obtained for a linear behavior $n = 1$ and a non-linear behavior with $n = 3$ by setting $\beta_{n=3} = \sqrt{\beta_{n=1}}$.

2.2. Evolution of the crystal rotation in response to deformation and recrystallization

As in [56, 57], the CTI constitutive law in the present model is coupled to an equation describing the rotation rate of the crystal orientation due to the deformation

$$\frac{\partial \mathbf{c}}{\partial t} = \mathbf{Wc} - \lambda [\mathbf{Dc} - (\mathbf{c}^T \mathbf{Dc}) \mathbf{c}], \quad (17)$$

where $\mathbf{W}(\mathbf{u}) = \frac{\nabla(\mathbf{u}) - \nabla^T(\mathbf{u})}{2}$ and $\mathbf{D}(\mathbf{u}) = \frac{\nabla(\mathbf{u}) + \nabla^T(\mathbf{u})}{2}$ are the spin- and strain-rate tensors. According to equation (17), the rotation of the \mathbf{c} -axis is due to the bulk spin, \mathbf{Wc} , and to the viscoplastic spin expressed by $\lambda [\mathbf{Dc} - (\mathbf{c}^T \mathbf{Dc}) \mathbf{c}]$. In the work of [56, 57], λ was set to 1. This value results from the hypothesis that the viscoplastic spin is only due to the contribution of the glide of dislocations on the basal plane, excluding any other glide planes (prismatic and pyramidal). This hypothesis has been widely made in previous studies [45, 58–61] and it is also taken here.

To take into account the impact of dynamic recrystallization on the evolution of the \mathbf{c} -axis orientation, we suggest adding a term to this equation, based on the assumption that dynamic recrystallization induces a local re-orientation of the \mathbf{c} -axis, either through the nucleation of a grain with a new orientation, or by the migration of a grain boundary, and that this re-orientation will lead to local softening.

We will express this dynamic recrystallization term together with the underlying assumption in section 2.3. When this term is added, the \mathbf{c} -axis rotation is described by:

$$\frac{\partial \mathbf{c}}{\partial t} = \mathbf{W}\mathbf{c} - \lambda [\mathbf{D}\mathbf{c} - (\mathbf{c}^T \mathbf{D} \mathbf{c}) \mathbf{c}] + \frac{1}{\Gamma_{RX}} (\mathbf{c}_0 - \mathbf{c}), \quad (18)$$

where Γ_{RX} is a parameter controlling the rate of rotation of the \mathbf{c} -axis toward an attractor, \mathbf{c}_0 , which represents the "ideal" orientation produced by recrystallization and whose formulation is described in section 2.3. The evolution of the orientation of the \mathbf{c} -axis is therefore controlled by the balance between (i) the deformation-induced rotation and (ii) a recrystallization-driven attractor, \mathbf{c}_0 .

The meaning of Γ_{RX} can be illustrated by considering the artificial case where only dynamic recrystallization contributes to the \mathbf{c} -axis rotation. In this case, equation (18) becomes $\frac{\partial \mathbf{c}}{\partial t} = \frac{1}{\Gamma_{RX}} (\mathbf{c}_0 - \mathbf{c})$. The norm of $\frac{\partial \mathbf{c}}{\partial t}$ can be interpreted as the rotation rate due to dynamic recrystallization only. This rate increases as $\|\mathbf{c}_0 - \mathbf{c}\|$ increases. Considering a constant \mathbf{c}_0 , the solution for the \mathbf{c} -axis rotation is:

$$\mathbf{c}(t) = (\mathbf{c}(0) - \mathbf{c}_0) e^{-\frac{t}{\Gamma_{RX}}} + \mathbf{c}_0. \quad (19)$$

In this case, the velocity of the rotation of \mathbf{c} towards \mathbf{c}_0 follows an exponential decay with a characteristic time Γ_{RX} , such that 95% (99%) of the rotation is obtained after $4\Gamma_{RX}$ ($5\Gamma_{RX}$). In the dynamic recrystallization model, \mathbf{c}_0 is not constant but depends on the local deviatoric stress tensor, \mathbf{S} .

2.3. Formulation of the recrystallization attractor \mathbf{c}_0

The formulation of \mathbf{c}_0 stems from the assumption that a grain (or part of a grain) rotates towards, or/and nucleates in, an orientation that facilitates the local plastic deformation. In other words, considering that the ice single crystal deforms mainly by dislocation glide on the basal plane, the recrystallization-induced rotation should maximize the Resolved Shear Stress (RSS) on the basal plane. The RSS for a dislocation with a Burgers vector \mathbf{a}_i (figure 1) gliding on the basal plane \mathbf{c} in response to a deviatoric stress \mathbf{S} is given by

$$RSS(\mathbf{a}_i, \mathbf{c}, \mathbf{S}) = \mathbf{S} : \boldsymbol{\mu}, \quad (20)$$

with $\boldsymbol{\mu} = \frac{1}{2} (\mathbf{c} \otimes \mathbf{a}_i + \mathbf{a}_i \otimes \mathbf{c})$.

In the CTI formulation, the behavior is isotropic in the basal plane, defined by the \mathbf{c} -axis. Therefore, defining the orientation for the maximum RSS means defining the orientation where the shear stress is maximum in the basal plane. Considering $s_1 > s_2 > s_3$ the eigenvalues and \mathbf{e}_i the corresponding eigenvectors of the deviatoric stress tensor \mathbf{S} , the maximum resolved shear stress is $|s_1 - s_3|$ and the associated orientations are [62]:

$$\mathbf{c}_0 = \frac{1}{2} (\mathbf{e}_1 \pm \mathbf{e}_3) \quad (21)$$

The attractor \mathbf{c}_0 not being unique for a given stress, an additional constraint must be formulated and fed to equation (18). Between the two possible values of \mathbf{c}_0 , we simply choose the one that is the closest to the actual \mathbf{c} axis in order to minimize the path between \mathbf{c} and \mathbf{c}_0 . Therefore, in practice, \mathbf{c}_0 is chosen so that the scalar product between \mathbf{c}_0 and \mathbf{c} is maximal.

2.4. CTI-RX- Model summary

The system of equations constituting the *CTI-RX* model is composed of:

- (1) The momentum equation under the Stokes assumption:

$$-\nabla \cdot \mathbf{S} + \nabla p = 0 \quad (22)$$

- (2) The non linear CTI law:

$$\begin{aligned} \mathbf{S} &= \eta_n^* (2\alpha_1 \mathbf{D} + 2\alpha_2 \mathbf{M}^D \text{Tr}(\mathbf{MD}) + \alpha_3 (\mathbf{MD} + \mathbf{DM})^D) \\ \eta_n^* &= 2\eta_n (\alpha_1 \text{tr}(\mathbf{D}^2) + \alpha_2 \text{tr}(\mathbf{MD})^2 + \alpha_3 \text{tr}(\mathbf{MD}^2))^{\frac{1-n}{2n}} \end{aligned} \quad (23)$$

- (3) The equation for the evolution of the \mathbf{c} -axis:

$$\frac{\partial \mathbf{c}}{\partial t} = \mathbf{Wc} - \lambda [\mathbf{Dc} - (\mathbf{c}^T \mathbf{Dc}) \mathbf{c}] + \frac{1}{\Gamma_{RX}} (\mathbf{c}_0 - \mathbf{c}), \quad (24)$$

with $\mathbf{c}_0 = \frac{\mathbf{e}_1 + \mathbf{e}_3}{2}$ where \mathbf{e}_i are the eigenvectors of \mathbf{S} and $|\mathbf{c} \cdot \mathbf{c}_0|$ is maximum.

3. Numerical scheme and implementation

The *CTI-RX* equations (section 2.4) are solved on a cuboid of polycrystalline ice submitted to uniaxial simple shear creep (section 3). A full field approach using FEM is chosen to describe the field of orientations \mathbf{c} at the element size. This implementation results in the *R³iCe* model (**R**heology, **R**ecrystallization, **R**heolef in **C**ontinuous Transverse Isotropic material). This design allows direct comparisons of texture evolution with existing laboratory creep experiments, in particular the ones performed by [28, 30, 31].

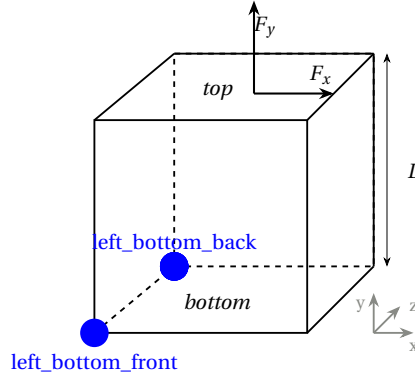


Figure 2. Schematic representation of the rectangular cubic simulation domain, with surface and point boundaries labeled.

3.1. Numerical experiments setups

3.1.1. Uniaxial creep tests

In this case, a zero vertical velocity ($u_y(\text{bottom}) = 0$) condition is applied at the bottom surface to simulate a fixed plateau, as in laboratory creep tests. To avoid translation of the sample, the position of one bottom summit is also fixed ($\mathbf{u}(\text{left_bottom_back}) = (0, 0, 0)$). To avoid rotation around the \mathbf{y} -axis, a zero-velocity condition is also applied on a second summit

($u_x(left_bottom_front) = 0$). The sample is deformed in uniaxial compression (or tension) by applying a constant normal stress on the top surface ($F_y(top) = F$). By convention, $F < 0$ ($F > 0$) corresponds to compression (tension). This Neumann condition leads to a non-uniform displacement over the surface as weaker elements may deform faster. This may hinder the direct comparisons with laboratory experiments or other numerical models. This issue is addressed in section 4.1.

3.1.2. Simple shear creep tests

In the simple shear tests, the forcing is applied as a constant tangential stress on the top boundary ($F_x(top) = F$) of the ice sample. Other boundary conditions are:

- $\mathbf{u}(bottom) = 0$,
- $u_y = u_z = 0$ for the lateral surfaces (left, right, front, back) to avoid solid rotation,
- $u_y(top) = u_z(top) = 0$.

3.2. Characteristic numbers and time

Adimensionalizing with respect to the material viscosity $\eta_n \sim Pa.s^{\frac{1}{n}}$, the vertical extent of the cuboid L (section 3) and the applied macroscopic stress $\Sigma \sim Pa$, the dynamical system of equations reads:

$$-\tilde{\nabla}\tilde{\mathbf{S}} + \tilde{\nabla}\tilde{p} = 0 \quad (25)$$

$$\begin{aligned} \tilde{\mathbf{S}} &= \tilde{\eta}_n^* (2\alpha_1 \tilde{\mathbf{D}} + 2\alpha_2 \mathbf{M}^D Tr(\mathbf{M}\tilde{\mathbf{D}}) + \alpha_3 (\mathbf{M}\tilde{\mathbf{D}} + \tilde{\mathbf{D}}\mathbf{M})^D) \\ \tilde{\eta}_n^* &= 2 \left(\alpha_1 Tr(\tilde{\mathbf{D}}^2) + \alpha_2 Tr(\mathbf{M}\tilde{\mathbf{D}})^2 + \alpha_3 Tr(\mathbf{M}\tilde{\mathbf{D}}^2) \right)^{\frac{1-n}{2n}} \end{aligned} \quad (26)$$

$$\frac{\partial \mathbf{c}}{\partial t} = \tilde{\mathbf{W}}(\tilde{\mathbf{u}}) \cdot \mathbf{c} - \lambda [\tilde{\mathbf{D}}(\tilde{\mathbf{u}}) \cdot \mathbf{c} - (\mathbf{c}^T \cdot \tilde{\mathbf{D}}(\tilde{\mathbf{u}}) \cdot \mathbf{c})] + \mathcal{M}o(\mathbf{c}_0 - \mathbf{c}) \quad (27)$$

where the superscript $(\tilde{\cdot})$ is used for all non-dimensional variables and operators.

The dimensionless number that arises when adimensionalizing the \mathbf{c} -axis evolution equation is $\mathcal{M}o$:

$$\mathcal{M}o = \left(\frac{\eta_n}{\Sigma} \right)^n \frac{1}{\Gamma_{RX}} \quad (28)$$

It is the ratio between a deformation characteristic time $\tau = \left(\frac{\eta_n}{\Sigma} \right)^n$ and the recrystallization characteristic time Γ_{RX} , which controls the rate of rotation of \mathbf{c} toward the attractor \mathbf{c}_0 . This adimensional number quantifies the relative weight of the contributions of recrystallization versus deformation to the rotation of the \mathbf{c} -axis.

3.3. Numerical algorithm

As the \mathbf{c} -axis evolution depends on the strain rate ($\tilde{\mathbf{D}}(\tilde{\mathbf{u}})$) and the effective viscosity η^* depends on both the strain rate and the \mathbf{c} -axis, the coupled equations (26) and (27) show non-linearity.

In order to solve this non-linearity system, linearization is performed.

The equation describing the evolution of the \mathbf{c} -axis is linearized using a second order backward differentiation formula (BDF2). Therefore, the time discretization of *CTI-RX* model gives:

$$-\tilde{\nabla}\tilde{\mathbf{S}}^{t+1} + \tilde{\nabla}\tilde{p}^{t+1} = 0 \quad (29)$$

$$\begin{aligned} \tilde{\mathbf{S}}^{t+1} &= \tilde{\eta}_n^{*t+1} \left(2\alpha_1 \tilde{\mathbf{D}}^{t+1} + 2\alpha_2 \mathbf{M}^{t+1D} Tr(\mathbf{M}^{t+1} \tilde{\mathbf{D}}^{t+1}) + \alpha_3 (\mathbf{M}^{t+1} \tilde{\mathbf{D}}^{t+1} + \tilde{\mathbf{D}}^{t+1} \mathbf{M}^{t+1})^D \right) \\ \tilde{\eta}_n^{*t+1} &= 2 \left(\alpha_1 Tr((\tilde{\mathbf{D}}^{t+1})^2) + \alpha_2 Tr(\mathbf{M}^{t+1} \tilde{\mathbf{D}}^{t+1})^2 + \alpha_3 Tr(\mathbf{M}^{t+1} (\tilde{\mathbf{D}}^{t+1})^2) \right)^{\frac{1-n}{2n}} \end{aligned} \quad (30)$$

$$\frac{3}{2\Delta t} \left(\mathbf{c}^{t+1} - \frac{4}{3} \mathbf{c}^t + \frac{1}{3} \mathbf{c}^{t-1} \right) = \tilde{\mathbf{W}}(\tilde{\mathbf{u}}^{t+1}) \cdot \mathbf{c}^{t+1} - \lambda \left[\tilde{\mathbf{D}}(\tilde{\mathbf{u}}^{t+1}) \cdot \mathbf{c}^{t+1} - (\mathbf{c}^{t+1})^T \cdot \tilde{\mathbf{D}}(\tilde{\mathbf{u}}^{t+1}) \cdot \mathbf{c}^{t+1} \right] + \mathcal{M}o(\mathbf{c}_0^{t+1} - \mathbf{c}^{t+1}) \quad (31)$$

The domain is spatially discretized using hexahedral Finite Elements. An initial \mathbf{c} -axis is prescribed for each element.

Finite elements and variational methods are used to solve the time-discretized problem on a Lagrangian grid within the C++ environment Rheolef [63]. The FE approximation for the tensorial mechanical parameter \mathbf{M} and the scalar mechanical parameter \mathbf{c} is P_0 . The FE approximation for the tensorial strain rate $\tilde{\mathbf{D}}$, spin rate $\tilde{\mathbf{W}}$ and stress $\tilde{\mathbf{S}}$ fields is P_1 . Therefore, the FE approximation for the displacement field needs to be P_2 .

Rheolef *problem_mixed* solver is used to solve the displacement field $\tilde{\mathbf{u}}$ and the pressure field \tilde{p} under the incompressibility hypothesis for the linearized version of equation (30) that is obtained by fixing the apparent viscosity η^* . A first fix loop is used to solved the non-linearity associated with η^* .

This first fix loop is nested in a second fix loop that solve the temporal evolution with the equation (31).

Algorithm 1 presents a pseudo code of the two nested fix points implemented in *R³iCe*. In practice, it is recommended for numerical efficiency to flatten the two nested fix loops. This algorithm is a semi implicit solver for the coupled equations (26) and (27). The simulated orientation field \mathbf{c} is thus consistent with the displacement field $\tilde{\mathbf{u}}$ and therefore with the deviatoric strain rate $\tilde{\mathbf{D}}$ and the deviatoric stress $\tilde{\mathbf{S}}$.

This implementation of *CTI-RX* model is distributed under *R³iCe* code.

3.4. CTI parameters values for ice single crystal

In this section, the choice of values for the CTI parameters, γ , η_n , n and β is explained (see equations (13) and (15)).

First, γ corresponds to the ratio of viscosities measured in compression and in tension for an ice single crystal that is well-oriented for basal slip. Laboratory experiments have shown that this ratio is very close to one, hence in our numerical simulations, we set $\gamma = 1$, as in previous studies [50, 51].

Following [8] and previous modeling works based on the CTI law [19, 48, 51], we set $n = 3$. While experiments in ice single crystals that are well-oriented for basal slip are best fitted by $n = 2$, experiments on crystals that are poorly-oriented for basal slip result in $n = 3$ [8] and a value of 3 must be imposed in the CTI formulation in order to recover $n = 3$ for the polycrystal response.

β is linked to the ratio between basal and non-basal shearing viscosities. [8] measured about four orders of magnitude ($\sim 10^4$ at 1 MPa) between the two values. This ratio is related to β through equation (16) $\beta^{\frac{n+1}{2}} = 10^4$. With $n = 3$, this leads to $\beta = 10^{-2}$: a value that matches those considered in previous studies based on the non-linear CTI formulation [19, 48, 51].

The viscosity η_n can be adjusted by comparison with the experimental response of the single crystal or that of isotropic polycrystals. The CTI law alone as been solved for axial compression creep of a single crystal oriented at 45° from the compression axis and of a polycrystal with random orientations picked from a uniform texture. The macroscopic strain rate is given by $\tilde{D}_{sc}^{sim} = 1.7 \times 10^{-2} \left(\frac{\eta_n}{\Sigma} \right)^n$ for the single crystal, and by $\tilde{D}_{px}^{sim} = 4.2 \times 10^{-5} \left(\frac{\eta_n}{\Sigma} \right)^n$ for the polycrystal. The viscosity η_n is obtained by comparing the simulated values to the experimental ones presented in [8] at 1 MPa ($D_{sc}^{exp} = [2 \times 10^{-5}, 2 \times 10^{-4}] s^{-1}$ for the single crystal, $D_{px}^{exp} = [9 \times 10^{-8}, 2 \times 10^{-7}] s^{-1}$ for the polycrystal). Thus $\eta_3^{sc} = [4.4, 9.4] MPa \cdot s^{1/3}$ for the single crystal and $\eta_3^{px} = [5.9, 7.7] MPa \cdot s^{1/3}$ for the polycrystal are obtained. Both values have overlapping range. The value of $6.0 MPa \cdot s^{1/3}$ for η_3 is chosen in the following.


```

1: Inputs:
    $\mathbf{c}^{init}$ 
2: Initialize:
    $\mathbf{c}^{-1} \leftarrow \mathbf{c}^{init}$ 
    $\mathbf{c}^0 \leftarrow \mathbf{c}^{init}$ 
    $\mathbf{u}^0 \leftarrow 0$ 
3: for  $t$  from 0 to  $N$  do ▷ Time evolution loop
4:    $k_c \leftarrow 0$ 
5:    $res_c \leftarrow +\infty$ 
6:    $\mathbf{u}^{t+1, k_c=0, k_{nl}=0} \leftarrow \mathbf{u}^t$ 
7:    $\mathbf{c}^{t+1, k_c=0} \leftarrow \mathbf{c}^t$ 
8:   while  $res_c > tol_c$  do ▷ Fix loop to solved (equation (31))
9:      $k_{nl} \leftarrow 0$ 
10:     $res_{nl} \leftarrow +\infty$ 
11:     $\mathbf{u}^{t+1, k_c, k_{nl}=0} \leftarrow \mathbf{u}^{t+1, k_c}$ 
12:    while  $res_{nl} > tol_{nl}$  do ▷ Fix loop to solved non linear CTI (equation (26))
13:       $H_n^* \leftarrow \eta_n^*(\mathbf{u}^{t+1, k_c, k_{nl}}, \mathbf{c}^{t+1, k_c})$  ▷ equation (26)
14:      find  $\mathbf{u}^{t+1, k_c, k_{nl}+1} \leftarrow \mathbf{u}^{t+1, k_c, k_{nl}+1}(H_n^*, \mathbf{c}^{t+1, k_c})$  ▷ problem_mixed solver on equation (26)
15:       $res_{nl} \leftarrow ||\mathbf{S}(\eta_n^*(\mathbf{u}^{t+1, k_c, k_{nl}+1}, \mathbf{c}^{t+1, k_c}), \mathbf{u}^{t+1, k_c, k_{nl}+1}, \mathbf{c}^{t+1, k_c}) - \mathbf{S}(H_n^*, \mathbf{u}^{t+1, k_c, k_{nl}+1}, \mathbf{c}^{t+1, k_c})||$ 
16:       $k_{nl} \leftarrow k_{nl} + 1$ 
17:    end while
18:     $H_n^* \leftarrow \eta_n^*(\mathbf{u}^{t+1, k_c, k_{nl}}, \mathbf{c}^{t+1, k_c})$ 
19:    compute  $\mathbf{S} \leftarrow \mathbf{S}(H_n^*, \mathbf{u}^{t+1, k_c, k_{nl}})$  ▷ equation (26)
20:    find  $\mathbf{c}_0 \leftarrow \mathbf{c}_0(\mathbf{S})$  ▷ equation (21)
21:    compute  $\mathbf{c}^{t+1, k_c+1} \leftarrow \mathbf{c}^{t+1, k_c+1}(\mathbf{c}_0, \mathbf{u}^{t+1, k_c, k_{nl}})$  ▷ equation (31)
22:     $res_c \leftarrow ||\mathbf{S}(\eta_n^*(\mathbf{u}^{t+1, k_c, k_{nl}}, \mathbf{c}^{t+1, k_c+1}), \mathbf{u}^{t+1, k_c, k_{nl}+1}, \mathbf{c}^{t+1, k_c+1}) - \mathbf{S}(H_n^*, \mathbf{u}^{t+1, k_c, k_{nl}}, \mathbf{c}^{t+1, k_c})||$ 
23:     $k_c \leftarrow k_c + 1$ 
24:  end while
25:   $\mathbf{u}^{t+1} \leftarrow \mathbf{u}^{t+1, k_c, k_{nl}}$ 
26:   $\mathbf{c}^{t+1} \leftarrow \mathbf{c}^{t+1, k_c}$ 
27: end for

```

Algorithm 1: Numerical algorithm, based on two nested fix loop: one for solving the viscosity, η_n^* , nested in a second one for solving for the temporal evolution of the orientation, $\dot{\mathbf{c}}$.

n	γ	β	η_n
3	1	10^{-2}	$6.0 \text{ MPa.s}^{1/3}$

Table 2. Parameters of the CTI law for the ice single crystal.

The parameters of the CTI law for the ice single crystal are summarized in table 2.

4. Validation of the CTI-based formulation for the viscoplastic response

In this section, we verify that The CTI law implemented in *R³iCe* correctly reproduces the mechanical response of the ice polycrystal. This is indeed a prerequisite before further enhancing the CTI formulation with a representation of DRX and its impact on texture evolution. This mechanical response is known to be characterized by strong strain and stress heterogeneities, which are very likely precursors of dynamic recrystallization [32]. In a first time, we therefore compare *R³iCe* predictions to that of the CraFT-EVP model [32], which is known to reproduce these stress-strain heterogeneities adequately [32, 64]. The *R³iCe* formulation should also correctly reproduce

texture evolution in absence of recrystallization. Since there are no experimental data for such evolution, as experimental conditions inevitably lead to dynamic recrystallization at bulk strains $> 1\%$, and to development of a DRX texture at strains $> 10\%$. The comparison will therefore be made with the predictions of a VPSC model that correctly matches observations along deep ice cores [12].

4.1. Stress and strain field predictions: a comparison with CraFT-EVP

The model CraFT-EVP (for CraFT-ElastoViscoPlastic) has been used to provide full-field predictions of the mechanical response of ice during primary and secondary creep [32]. It is based on an elasto-viscoplastic formulation proposed by Suquet et al. 2012 [65] and solved using the CraFT software. The predictions of CraFT-EVP for the mechanical response as well as stress and strain fields were validated by direct comparisons with mechanical tests on ice polycrystals that included strain fields measurements by Digital Image Correlation [32, 65]. Stress and strain fields predicted at secondary creep, prior to any texture evolution owing to DRX, were in good agreement with experimental observations at 1% strain. With no texture evolution, CraFT-EVP and $R^3 iCe$ both simulate a stationary secondary creep.

The CraFT-EVP predictions will therefore be used in the following to evaluate the relevance of the fields predicted by $R^3 iCe$ prior to DRX-induced texture evolution. Reproducing accurate stress fields in $R^3 iCe$ is key since the recrystallization attractor \mathbf{c}_0 depends on the deviatoric stress S at the element scale. Please note that the calibration for the CTI law in $R^3 iCe$ is done independently (section 3.4) and is not fitted to CraFT-EVP results.

Figure 3(a-b) shows the polycrystal microstructure generated by a Voronoi Tessellation using Neper [66] used for both CraFT-EVP and $R^3 iCe$ simulations. In this configuration, referred thereafter as *grains microstructure*, grains are defined as a group of connected elements that share the same initial orientation. Figure 3(c) shows a microstructure in which orientations are defined at the mesh level. For this microstructure, there is no grain in the sense of a group of connected elements that share the same orientation. Such configuration is referred as *no-grain* thereafter.

Figure 4 shows the component ε_{yy} of the strain field and the component σ_{yy} of the stress field for the three uniaxial creep tests along the \mathbf{y} -axis after 1% of macroscopic compressive strain. The simulated strain field compares reasonably well between CraFT-EVP and $R^3 iCe$. Location of areas in compression (blue) and in extension (red) are similarly prescribed (figure 4(b)). On the *grains microstructure* significant differences between the responses of the models CraFT-EVP and $R^3 iCe$ are restricted to the first layers of grains close to the top surface and result from the different boundary conditions applied in the two models. In $R^3 iCe$, the Neumann boundary condition on the top surface results on a force applied on each elements that can lead to heterogeneous displacement on this surface. As a result, some "weaker" grains are deforming more, as represented by the dark blue areas on figure 4(b). In CraFT-EVP, periodic boundary conditions are imposed owing to the fact that equations are solved with a Fast Fourier Transform-based method. The simulated stress fields (figure 4(a)) compare satisfactorily in terms of amplitude and global pattern although the precise stress localisations show more scattering. Some of this mismatch may also be explained by the differences in boundary conditions between the two models. Observed stronger stress and strain concentrations in CraFT-EVP results from the higher mesh resolution ($\sim \times 8$).

The distributions of the equivalent stress and the equivalent strain (figure 5) compare relatively well when considering the impact of boundary conditions just mentioned for the *grains* configuration. This discrepancy almost vanishes in the *no-grain* configuration, where the impact of boundary conditions is reduced. Indeed, the Neumann boundary conditions has less of an impact, as more different orientation-elements are in contact with the top surface. In particular, the

stress-field distribution for the *no-grain* configuration is similar to the CraFT-EVP one simulated with the *grains microstructure*. Distribution for all components of both tensors $(\varepsilon_{ij}, \sigma_{ij})$ is given in appendix B.

To summarize, CraFT-EVP taken as a reference, strain and stress fields seem correctly reproduced by $R^3 iCe$ at secondary creep. In the following, all simulations are performed using the *no-grain* configuration in order to use a larger number of orientations with reasonable computation times. As stress and strain fields compare reasonably well between the *grains* and *no-grain* configuration this choice should have a limited impact on the simulated stress fields and therefore on the evaluation of the attractor \mathbf{c}_0 .

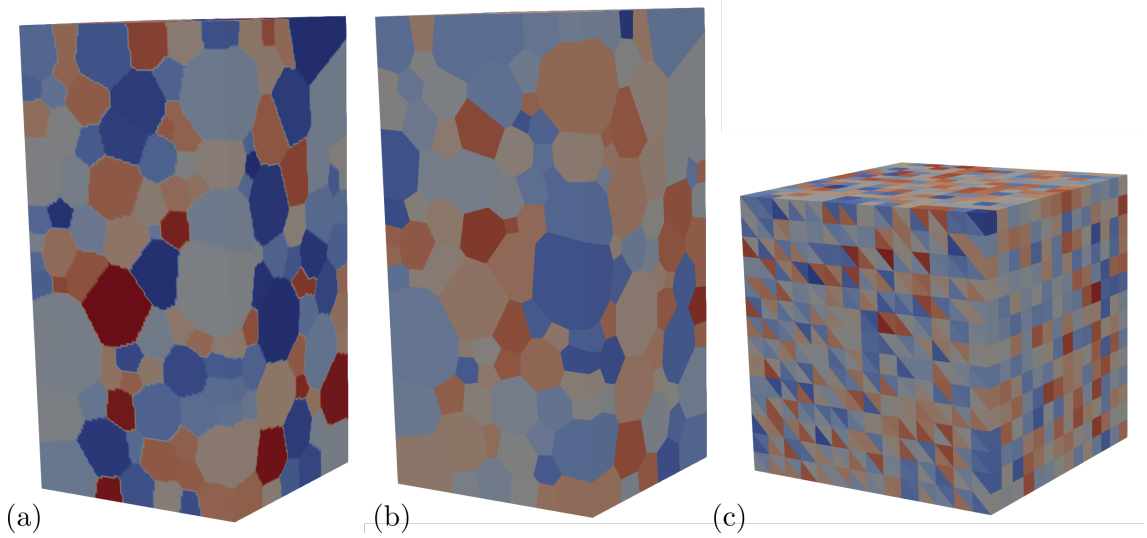


Figure 3. (a) Microstructure generated via a Voronoi tessellation using Neper. It is used in CraFT-EVP model (b) Same microstructure meshed for $R^3 iCe$ with tetrahedral elements. (c) Microstructure in which orientations are defined at the element scale on a hexahedral mesh. The color are used to highlight the different grains and are not related to any physical property.

4.2. Deformation textures

In $R^3 iCe$, the texture evolves by rotation of the \mathbf{c} -axes due to deformation and recrystallization. By setting \mathcal{M}_o to 0 in equation (18), dynamic recrystallization is inhibited and the texture evolution, defined by the rotation of the \mathbf{c} -axes in the polycrystal is solely controlled by the viscoplastic deformation. The predictions can then be compared with previous simulations of the texture evolution in ice polycrystals performed using the mean-field VPSC approach [12, 67], which correctly reproduce the textures measured along ice cores in the depth range where dynamic recrystallization is supposed to be a second order process.

Uniaxial compression tests under a 1 MPa deviatoric stress were performed using the *no-grain* configuration with initial orientations randomly picked from a uniform texture.

Figure 6(a) presents the evolution with strain (i.e. time) of the eigenvalues $(a_i, i = 1, 3)$ of the second order orientation tensor $(\mathbf{a}^{(2)} = \frac{1}{N} \sum_{i=0}^N \mathbf{c}_i \otimes \mathbf{c}_i)$, the strain rate and the texture in the Z plane

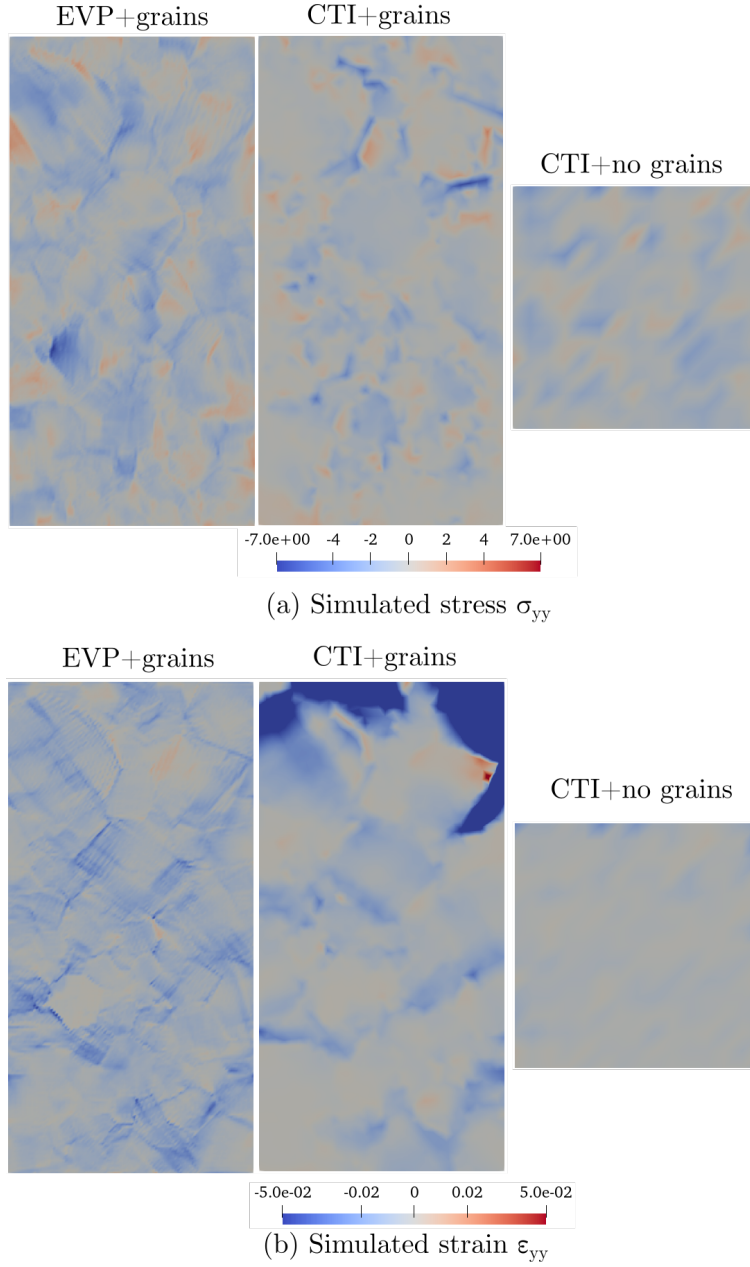


Figure 4. Comparison of predicted (a) stress ($\sigma_{22} = S_{22} + p$) and (b) strain (ϵ_{22}) fields for the "grain" microstructure using CraFT-EVP and $R^3 iCe$ and for a "no-grain" microstructure using $R^3 iCe$.

(perpendicular to the compression direction). Figure 6(d) shows textures predicted at 22%, 40% and 60% total strain.

A strong cluster (single maximum of **c**-axes) texture develops as strain increases and this induces geometrical hardening of the polycrystal. Strain-rate decrease of a factor ~ 1.5 is predicted between 20% and 60% total strain, when the texture is highly clustered ($a_1 \approx 0.71$).

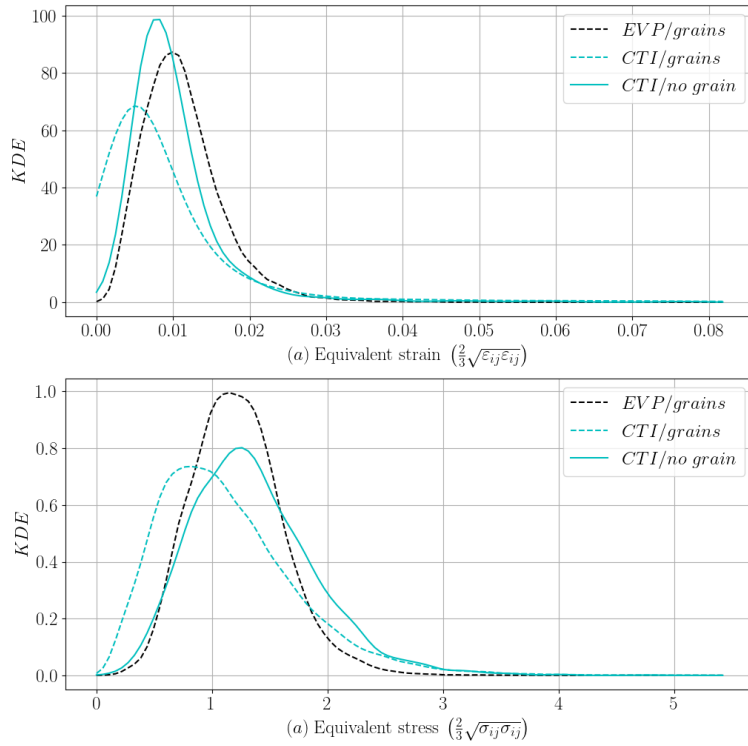


Figure 5. Kernel Density Estimation of the equivalent strain (a) and equivalent stress (b) fields simulated with CraFT-EVP (EVP, black line) and R^3iCe (CTI, cyan line). The dashed lines show results obtained for simulations where grains are defined by multiple mesh elements (*grains* microstructure) (figure 3 a-b). The full line shows a R^3iCe simulation where a single orientation is attributed per element (*no-grain* microstructure) (figure 3 c)

Similar cluster textures are observed along deep cold ice cores, for instance along the Talos Dome ice core [12] where a clustered texture with $a_1 \approx 0.7$ was measured at about 650 *m* depth, where an accumulated strain of 60% is estimated. A similar texture is predicted using a ViscoPlastic Self Consistent (VPSC) model at 60% total shortening when departing from an isotropic texture [12].

5. Texture evolution with recrystallization: comparison with experimental data

The aim of this section is to test the ability of the R^3iCe model to predict the evolution of the **c**-axes orientation due to both deformation and dynamic recrystallization (equation (27)) and, hence, to predict the texture development under uniaxial compression, uniaxial tension and simple shear by comparison with experiments performed under similar conditions.

The laboratory creep experiments selected to validate the model are:

- Uniaxial compression experiments from [28] ($\Sigma \sim 0.7 \text{ MPa}$, $T = -5^\circ \text{C}$)
- Uniaxial tension experiments from [26] ($\Sigma \sim 0.4 \text{ MPa}$, $T = -3^\circ \text{C}$)
- Torsion experiments from [31] ($\Sigma_{max} \sim 0.5 \text{ MPa}$, $T = -7^\circ \text{C}$),

where Σ stands for the macroscopic applied stress and Σ_{max} corresponds to maximum stress resulting from the applied torque.

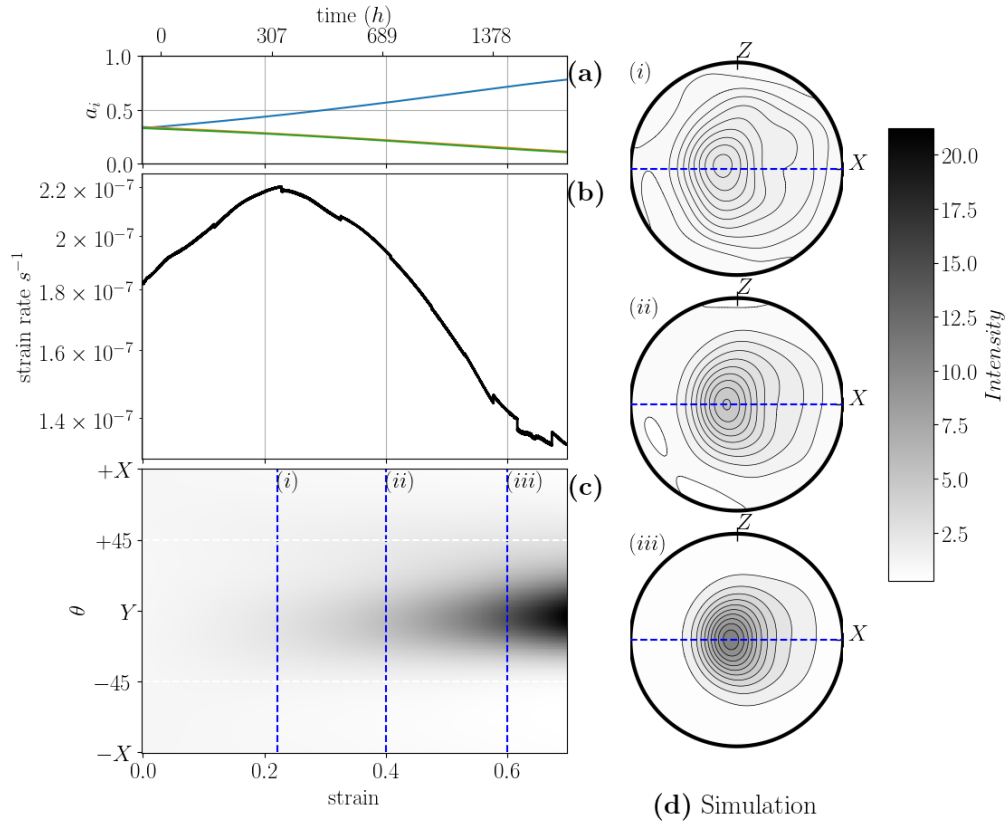


Figure 6. Simulation of uniaxial compression along Y with no recrystallization $\Gamma_{RX} = +\infty$, $Mo = 0$. a) Evolution with strain of the eigenvalues of the second order orientation tensor ($a_1 > a_2 > a_3$); b) evolution with strain of the macroscopic strain rate; c) evolution of the intensity of the texture with the colatitude θ over a section defined on the Z plane (dashed blue lines in d)). Data at 22%, 40% and 60% macro strain are shown. The white dashed lines define the angle at $\pm 45^\circ$ from the compression axis Y ; d) textures presented as pole figures for 22% (i), 40% (ii), and 60% (iii) macro strain. All figures presenting texture data are color-coded using the same colorbar, which is displayed on the right.

The model predictions are also compared with strain-controlled uniaxial compression tests under confining pressure performed by [30]. These conditions enabled to reach higher flow stresses without failure ($\Sigma \sim [1.3, 4.3] \text{ MPa}$, $T = -10^\circ \text{C}$) and it will allow us to test the predictions in a wider range of configurations.

For each stress configuration, simulations using the *no-grain* configuration are performed starting with initial orientations randomly picked in a uniform texture. The parameters for all simulations are given in table 3. For all configurations, the simulated texture evolution is represented by (1) the evolution of the eigenvalues a_i of the second order orientation tensor $\mathbf{a}^{(2)}$ as defined in section 4.2, (2) pole figures representing the \mathbf{c} -axes distribution at various strains, and (3) the evolution with strain of the texture in a section extracted from the pole figure. These outputs are compared with the pole figures obtained during the experiments at three selected strain values. The simulated strain-rate evolution is plotted to evaluate the enhancement factor associated with the texture evolution.

References	Model inputs		Physical values		
	Stress	$\mathcal{M}o$	Σ (MPa)	Γ_{RX} (days)	T (°C)
Montagnat et al. 2015 [28]	Compression	8.10×10^{-4}	0.7	8.7	-5
Jacka et al. 1984 [26]	Tension	2.96×10^{-5}	0.4	3.4	-3
Journaux et al. 2019 [31]	Simple Shear	8.33×10^{-4}	0.5	24.0	-7
Qi et al. 2017 [30]	Compression	$[37.9, 1.05] \times 10^{-5}$	[1.3, 4.3]	3	-10

Table 3. Values of the numerical and physical parameters used in the model R^3iCe .

5.1. Simulation of texture evolution in uniaxial compression

Results presented in figure 7 were obtained under an imposed compressive stress of 0.7 MPa in the **Y** direction. They are compared with experimental measurements from Montagnat et al. 2015 [28] performed on isotropic granular ice at -5°C , under a constant force with initial stresses of 0.7 and 0.8 MPa up to various strains (from 2 to 17.8% bulk shortening).

Comparison of the **c**-axis pole figures shows a good qualitative agreement between the simulated and the experimental textures (figure 7(d-e)). Both evolve from a girdle texture with a cone angle at 45° to the compression axis to a more concentrated girdle with cone at 35° to the compression axis. A nearly constant cone opening is reached at $\sim 20\%$ strain (figure 7(d)) There is also a good agreement between the predicted evolution of the eigenvalues of the texture and those measured at 7%, 12% and 17.8% (figure 7(a)).

This good agreement between experimental and simulated textures was obtained for a value of $\Gamma_{RX} = 8.7$ days. During the experiments, 17.8% strain was reached after 144 hours (~ 6 days). In the model simulations, this strain is reached in a shorter time (~ 100 hours)

The macroscopic response predicted by R^3iCe shows a clear softening associated with the development of the texture. A maximum enhancement factor (EF) of 4.8 is obtained at $\sim 19\%$ strain (black arrow, figure 7), which corresponds to a girdle texture with the cone angle at around $\sim 45^\circ$ to the compression axis. This softening is followed by a slight hardening as the girdle texture slowly evolves towards a cone angle at $\sim 35^\circ$ to the compression axis.

The bulk strain associated with the maximum strain rate and the simulated enhancement factor cannot be directly compared to that measured in Montagnat et al. 2015 [28] because these experiments were performed under constant force and the area of the sample section evolved during the tests, whereas the model simulations are performed in a constant stress configuration. The simulated strain rate may be corrected by assuming a constant sample volume during the experiment, what leads to $\dot{\epsilon}_{sim}^{corr} = \dot{\epsilon}_{sim} \times (1 + \epsilon)^3$. This corrected strain rate is plotted in blue in figure 7(b). It brings the maximum strain rate to $\sim 10\%$ and the enhancement factor at a value of 3.2. These values are closer to the macroscopic response measured by Montagnat et al. [28] characterized by an enhancement factor between 3.3 to 3.8.

5.2. Simulation of texture evolution in uniaxial tension

Experimental creep tests performed in uniaxial tension are scarce. Jacka et al. 1984 [26] present one experiment performed at -3°C , up to 9.3% octahedral shear strain that corresponds, following the definition given in Jacka et al. 1984 [68], to 13.1% axial strain. At this strain level, they did not attain the quasi-constant strain-rate typical of tertiary creep. The texture obtained, measured by the classical Rigsby stage technique with one orientation per grain, is presented in figure 8. The texture is characterized by a small circle girdle with a mean half angle of 50.4° and a standard deviation of 15.3° . Although tertiary creep was not reached in this experiment, an enhancement factor of ~ 3 , similar to the one observed in compression in the same conditions, is measured.

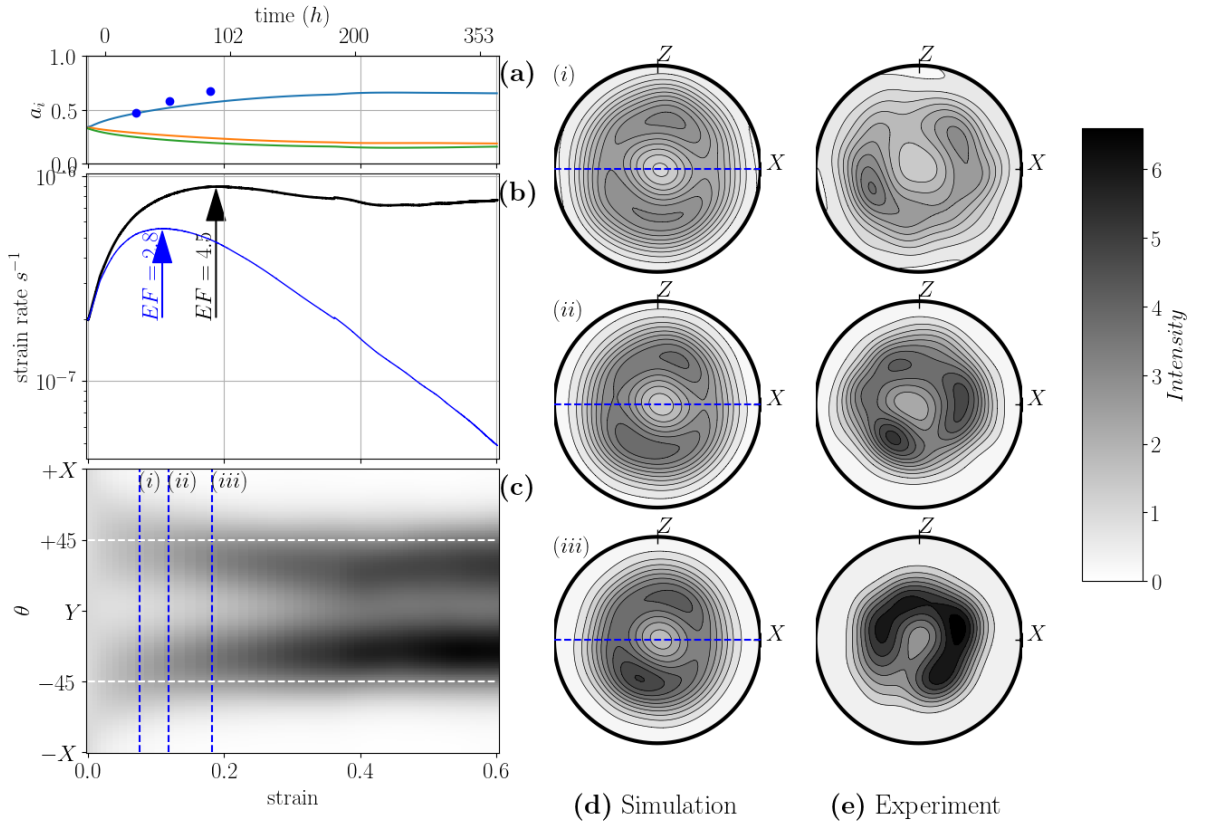


Figure 7. Simulations for the case of uniaxial compression creep along the Y direction with parameters from table 3 and comparison with experimental data. a) Evolution with strain of the eigenvalues of the second order orientation tensor ($a_1 > a_2 > a_3$). The blue dots correspond to experimental values from [28]; b) simulated macroscopic strain rate (black) and corrected simulated macroscopic strain rate (blue) to match a constant force boundary conditions instead of the constant stress one used in the simulation. EF stands for Enhancement Factor; c) evolution with strain of the intensity of the texture with the colatitude θ over a section defined on the Z plane (dashed blue lines in (d)). Data at 7%, 12% and 17.8% macro strain are shown. The white dashed lines define the angle at $\pm 45^\circ$ from the compression axis Y ; d) simulated textures (pole figures) for 7% (i), 12% (ii), and 17.8% (iii) macroscopic strain; e) measured textures for the same macroscopic strains [28]. All figures presenting texture data are color-coded using the same colorbar.

The texture evolution and macroscopic response predicted by a simulation under uniaxial tension creep are shown in figure 9. The texture evolves with increasing strain towards a girdle texture with a cone at an angle slightly larger than 45° to the extension direction. This texture seems to stabilize at $\sim 10\%$ axial strain. An enhancement factor of about 6.6 is simulated at 13% axial strain.

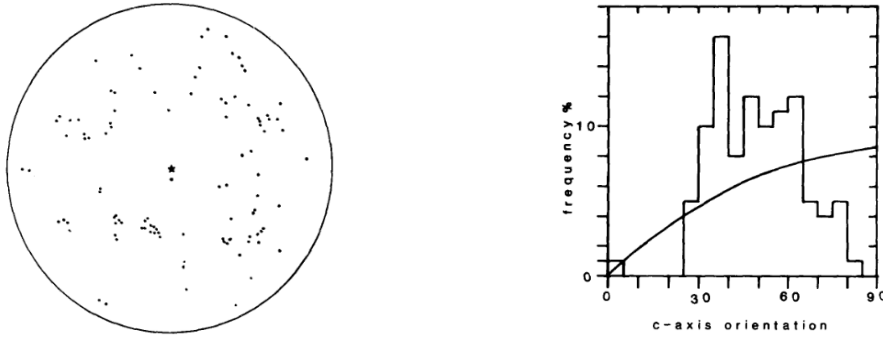


Figure 8. Texture obtained after 9% of octahedral tension strain (about 13% axial strain) performed at -3°C with an octahedral stress of 0.4 MPa . The star \star in the centre of the pole figure shows the direction of the tension axis. From Jacka et al. 1984 [26].

5.3. Simulation of texture evolution in simple shear.

The simulated texture evolution in simple shear is compared with observations made by Journaux et al. [31] for torsion experiments on isotropic granular ice. Experiments were performed at -7°C , under a constant torque corresponding to a maximum shear stress between 0.4 and 0.6 MPa.

The experimental textures are characterized by two sub-maxima, one almost perpendicular to the shear plane, called $M1$ and the second one, $M2$, initially at low angle to the shear plane. Similar evolutions were also observed in simple shear by [25, 41, 69]. As shear strain increases, $M2$ merges with $M1$ to form a highly concentrated cluster texture characterized by a single maximum of \mathbf{c} -axes normal to the shear plane. The simple shear simulations performed here reproduce this evolution relatively well, as shown in figure 10.

By accounting for dynamic recrystallization, the R^3iCe model is able to reproduce the evolution of both $M1$ and $M2$ maxima with strain. At low shear strains ($\gamma \sim 0.2$), $M1$ concentrates normal to the shear plane while $M2$ follows the principal extension direction (white dashed line, figure 10(c) bottom and figure 10(d)). As strain increases, $M2$ rotates towards $M1$. At a shear strain of 2, the texture is characterized by an elongated single maximum of the \mathbf{c} -axis normal to the shear plane as $M1$ and $M2$ are merging. The evolution of the intensity of the eigenvalues of the second order orientation tensor are also well reproduced (figure 10(a)).

The strain rate increases rapidly up to $\gamma = 0.5$ while the double-maxima texture develops (figure 10(d)). It continues to increase, but at a progressively slowing rate as the texture evolves towards a single maximum normal to the shear plane, up to $\gamma \sim 3.5$ where it reaches a quasi-steady state.

In phase with Treverrow et al. 2012 [37], we define an enhancement factor for simple shear as being the ratio between the strain rate during secondary creep (here it corresponds to the beginning of the run) and the one associated with the strongest simulated texture. The latter value is conceptually similar to the secondary creep rate that should be measured for a similar simple shear simulation with the strongest simulated texture as the initial texture. Doing so, we measure an enhancement factor (EF) of 7.1 that matches Treverrow et al. 2012 [37] measurements for an equivalent applied shear stress.

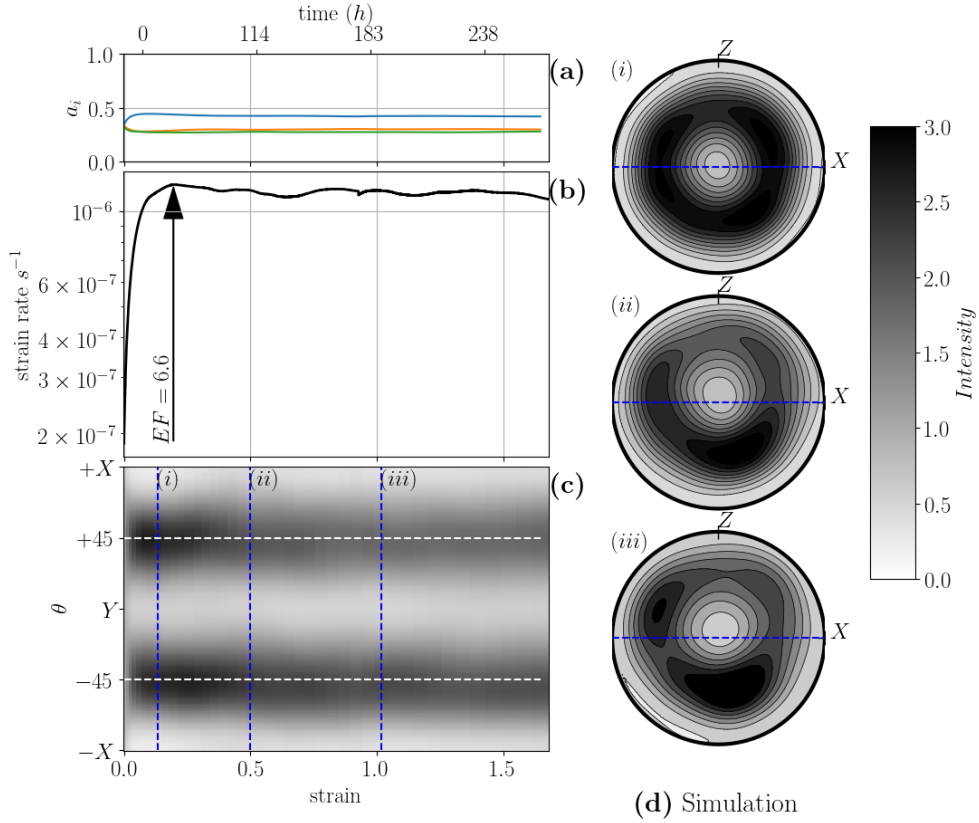


Figure 9. Simulations for the case of uniaxial tension creep along the Y direction with parameters from table 3 and comparison with experimental data. a) Evolution with strain of the eigenvalues of the second order orientation tensor ($a_1 > a_2 > a_3$); b) simulated macroscopic strain rate. EF stands for Enhancement Factor; c) evolution with strain of the intensity of the texture with the colatitude θ over a section defined on the Z plane (dashed blue lines in d)). Data at 13%, 50% and 100% axial macro strain are shown. The white dashed lines define the angle at $\pm 45^\circ$ from the compression axis Y ; d) simulated textures (pole figures) for 13% (i), 50% (ii), and 100% (iii) axial macro strain. All figures presenting texture data are color-coded using the same colorbar.

5.4. Testing the relative effect of deformation and recrystallization under higher stresses

The work of Qi et al. [30] provides some highly resolved textures obtained in conditions (temperature, type of samples) similar to the ones employed here, however under imposed displacement rates that induce higher stress conditions (see table 3). The stress values reported in table 3 correspond to the flow stress, i.e. the nearly constant stress reached after peak stress, at about 20% strain. To reach deviatoric stresses higher than 1 MPa without failure a confining pressure of 10 MPa was applied.

To test the sensitivity of the dynamic recrystallization formulation to the level of stress, we performed simulations under creep conditions with the stress values from Qi et al. 2017 [30] experiments. As $CTI-RX$ equations are relating the deviatoric stress to the deviatoric strain and are solved under Stokes hypothesis (incompressibility), it is not necessary to numerically apply the confining pressure. Although both boundary conditions differ between the simulations (macro-

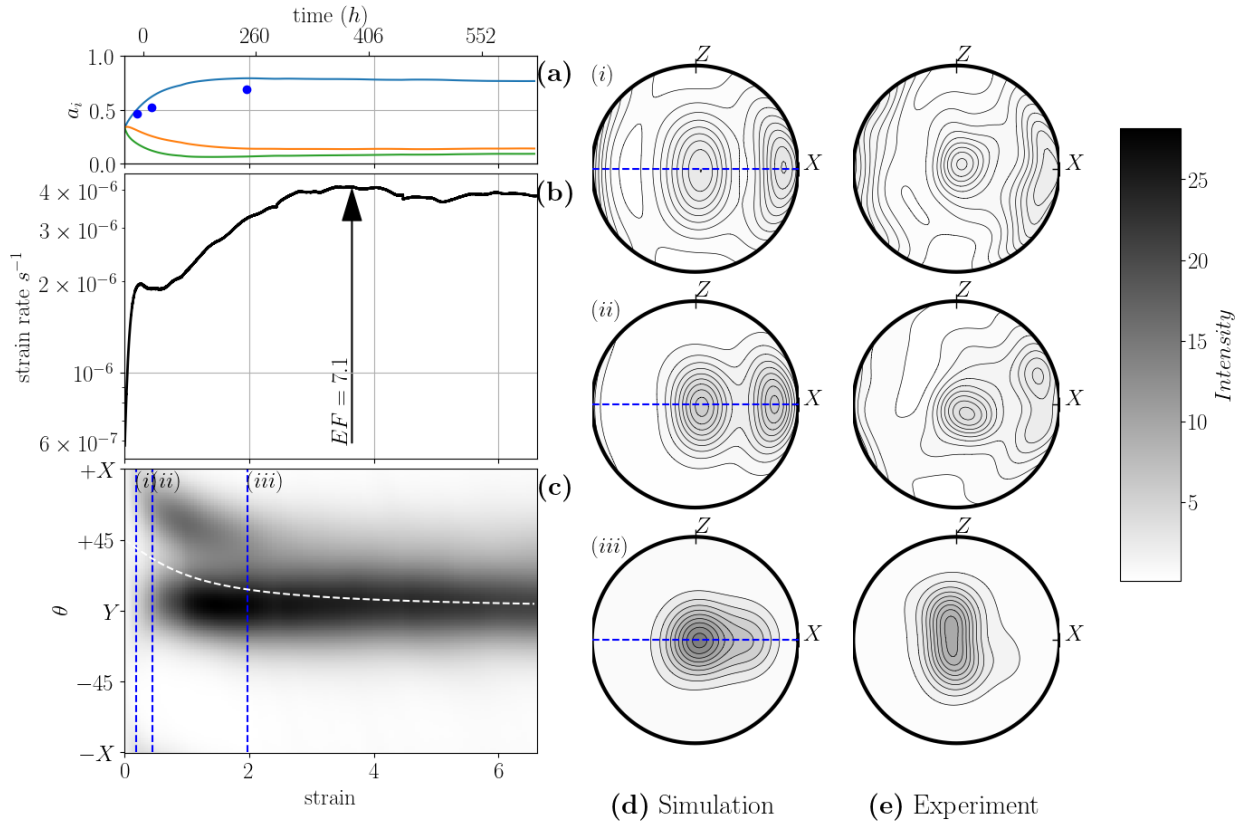


Figure 10. Simulations for the case of simple shear creep test (shear plane normal to the Y -axis and shear direction parallel to X) with parameters from table 3 and comparison with experimental data. a) Evolution with strain of the eigenvalues of the second order orientation tensor ($a_1 > a_2 > a_3$). The blue dots correspond to experimental values from Journaux et al. 2019 [31]; b) simulated macroscopic strain rate. EF stands for Enhancement Factor; c) evolution with strain of the intensity of the texture with the colatitude θ over a section defined on the Z plane (dashed blue lines in d)). Data at $\gamma = 0.2, 0.42$ and 1.96 are shown. The white dashed line follows the orientation of the principal extension axis; d) simulated textures (pole figures) $\gamma = 0.2$ (i), $\gamma = 0.42$ (ii) and $\gamma = 1.96$ (iii); e) measured textures for the same macroscopic shear strains [31]. All figures presenting texture data are color-coded using the same colorbar.

scopic constant stress) and experiments (macroscopic constant displacement rate), we assumed the quasi-steady state behavior sampled by the flow stress measurements in the experiments to be equivalent to the quasi-steady state part of the tertiary creep in the creep simulations [70]. Stable textures expected at both stages can therefore be compared.

The comparison between simulated and observed textures at different compressive flow stresses is shown in figure 11. The experimental observations are well reproduced. Both measured and simulated textures show a transition from a girdle texture to a weak single maximum with increasing flow stress for a macroscopic strain of $\sim 20\%$. To correctly fit the experimental data, a value of Γ_{RX} of 3 days is used, which is lower than the one used to reproduce the unconfined

compression creep tests of Montagnat et al. 2015 [28] (table 3). This implies a higher relative contribution of recrystallization compared to deformation at higher stresses.

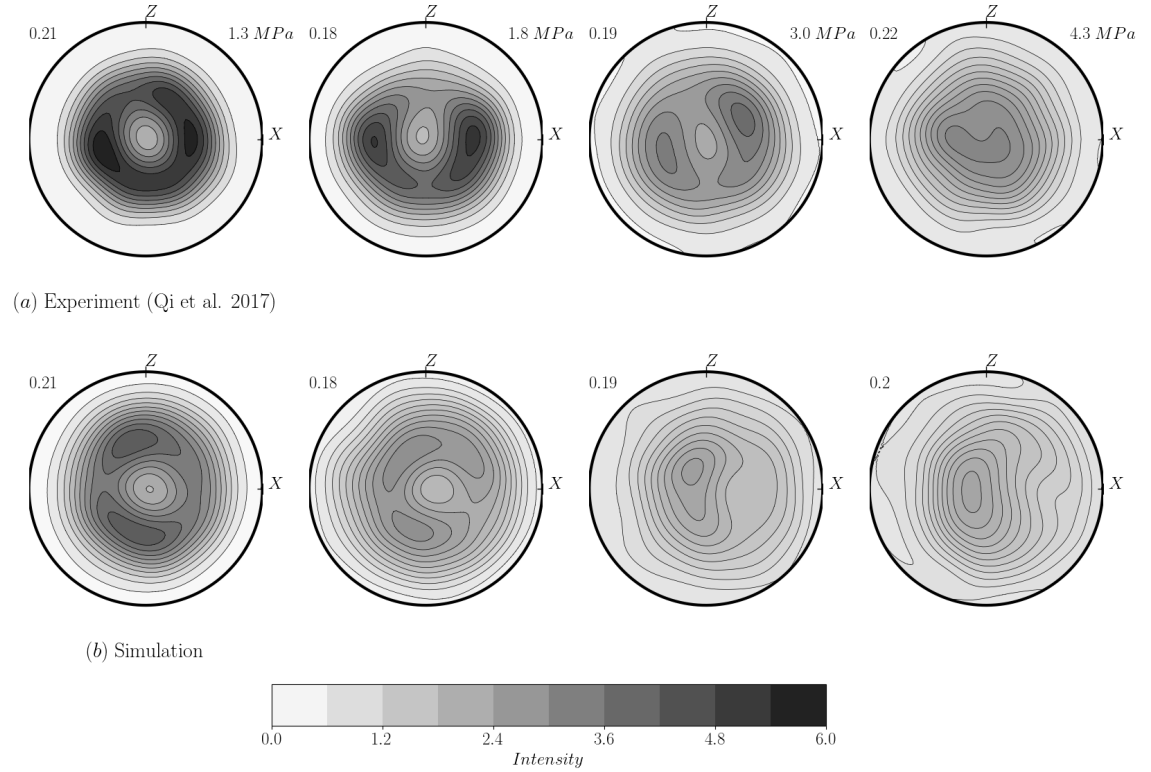


Figure 11. Simulation of uniaxial compression creep test along Y . Comparison between $R^3 iCe$ predictions and experiments by Qi et al. [30]. (a) Textures from [30] obtained by EBSD for various strain rates leading to different quasi-steady state compressive flow stress (top right) at macroscopic strains of $\sim 0.2\%$ (actual strains indicated at the top left of each pole figure). (b) Simulated textures developed in creep simulation under the same compressive stress at the same macroscopic strains.

6. Discussion

The *CTI-RX* model presented here enables the simulation of texture evolution in polycrystalline ice, as shown in the simulations in compression, simple shear and tension, including or not dynamic recrystallization. Without recrystallization, the texture evolution predicted by the model reproduces correctly natural textures observed along deep ice cores where dynamic recrystallization is supposed to have a low impact.

The novelty of the present model, and its implementation, stands on the simulation of the evolution of the orientation of c -axes based on a new formulation that (i) introduces an attractor controlled by the local stress field to reproduce the impact of DRX mechanisms (ii) is coupled with the CTI law in order to take into account the strain and stress field heterogeneities at the crystal scale arising from the crystal viscoplastic anisotropy, (iii) solves these coupled equations

using an semi-implicit numerical scheme in a full field implementation using FEM, ensuring consistency between texture evolution and mechanical behavior. The first two ingredients derive from experimentally-based knowledge of dynamic recrystallization processes.

Indeed, recent experimental observations have (i) clearly documented the role of the crystal viscoplastic anisotropy in generating local stresses and strains markedly different from the macroscopic ones [29, 32, 64] and (ii) revealed that the formation of new orientations (nucleation) during dynamic recrystallization occurs through bulging (heterogeneous grain boundary migration) and polygonization (formation of new grains boundaries by organization of dislocations within a grain) [29, 33, 64, 71, 72]. These two processes are controlled by the local strain and stress fields and result in recrystallized orientations that are strongly related to, but slightly different from, the parent grains orientations. The last important experimental observation is that the development of recrystallization textures leads to the weakening of the polycrystal mechanical response. All these observations justify the choice of a continuous formulation for the \mathbf{c} -axis orientation evolution (equation (18)), with a targeted recrystallized orientation that is calculated so that to maximize the local basal resolved shear stress (equation (21)).

Comparison with tertiary creep experiments made in compression [28, 37, 39], in simple shear [31, 37, 41] and in tension [26] supports the fact that the R^3iCe model is able to reproduce texture evolution in conditions similar to those of laboratory experiments ($T = -5$ to -10°C , $S \sim 1\text{ MPa}$). For that, a single parameter is adjusted: the recrystallization parameter Γ_{RX} , which weights the relative contribution of deformation and recrystallization to the rotation of the \mathbf{c} -axes. As expected, at e.g. similar stress conditions, a lower temperature requires a higher Γ_{RX} value (and therefore a lower weight of dynamic recrystallization) to correctly reproduce the experimental texture evolution. In particular, the two-maxima texture measured in simple shear (in natural and laboratory ice) is correctly reproduced here, together with the kinetics of its evolution with strain toward a single-maximum cluster.

Simulations at higher uni-axial compressive stresses (from 1 to 4 MPa) have been performed to compare with the experiments of Qi et al. 2017 [30]. Contrary to previously mentioned experiments, these latter were performed under a range of imposed strain-rate conditions resulting in variable flow stresses. A confining pressure of 10 MPa was applied to prevent from failure at the relatively high strain rates considered. A higher strain rate results in a greater relative impact of deformation versus DRX on the texture. This leads to more clustered textures at higher flow stress. From this perspective, R^3iCe run under imposed stress without confining pressure is able to correctly represent the texture clustering with stress. Indeed, experimental textures measured at 20% strain are satisfyingly reproduced by R^3iCe providing that Γ_{RX} is given a relatively low value (3 days for $T = -10^\circ\text{C}$) compared to the one determined for unconfined creep compression experiments (8.7 days for $T = -5^\circ\text{C}$). This low value of Γ_{RX} indicates that, in the simulations, a high amount of recrystallization is necessary to reproduce the experimental textures and to counterbalance the impact of deformation on the \mathbf{c} -axes rotation. We interpret this apparent contradiction as follows. Kalifa et al. [73] performed triaxial tests under the same range of strain rate ($\sim 10^{-5} - 10^4\text{ s}^{-1}$) than Qi et al. 2017 [30] and under a confining pressure varying from 0 to 10 MPa. By careful observations made right after the peak stress, they estimated the density of cracks in the microstructure and revealed that micro-cracks were visible up to 10 MPa confining pressure. Micro-cracking is therefore to be expected during Qi et al. 2017 [30] experiments. Strong stress concentration happens at crack tips and Chauve et al. 2017 [72] have recently shown that, for ice, it can be released through active recrystallization mechanisms taking place in the crack area. R^3iCe formulation is not able to take into account micro-cracking at high stress and strain-rate conditions, neither the impact of a confining pressure. The account for the enhancement of recrystallization due to plastic energy available around crack tips is made by increasing the recrystallization rate (Γ_{RX}).

For all conditions simulated with R^3iCe , we show that the *CTI-RX* model reproduces accurately the softening at the transition from secondary to tertiary creep. The kinetics of the transition and the resulting enhancement factors, when departing from an isotropic texture, are correctly simulated as well, as compared with experimental results performed in similar conditions [21, 26, 28, 36, 37]. Since the present model does not consider any softening mechanism associated with dislocation interactions or grain boundary migration, this comparison seems to confirm that texture-induced viscoplastic anisotropy explains most of the mechanical softening measured during tertiary creep. Therefore, the softening associated with dislocations annihilation and grain boundary migration during dynamic recrystallization seems to play a secondary role.

Recent models of texture evolution during dynamic recrystallization have been proposed by Rathmann et al. 2021 [54] and Richard et al. 2021, 2022 [47, 74], aiming to account for texture-induced anisotropy of ice in large-scale models. Their formulation is based on an Orientation Distribution Functions (ODF) in which dynamic recrystallization is represented by two terms: one term that accounts for the production of orientations based on a given parameter, the *deformability*, that is calculated using the Sachs constant stress assumption, and a second term that accounts for the diffusion of orientations. Although this approach is not intended to prescribe the mechanical response evolution due to texture development, it can be compared to the *CTI-RX* formulation. The *deformability* term can be obtained from equation (18) by assuming homogeneous stresses (Sachs model). The diffusive term is necessary to reproduce the texture dispersion effect owing to recrystallization. This is spontaneously obtained in full-field approaches such as R^3iCe , due to the heterogeneous stress field. Although these models accurately predict steady-state textures for different strain geometries, the predictions for transient textures evolution are less accurate than that from R^3iCe . This highlights the fundamental role of stress heterogeneities in texture evolution during the transition between secondary and tertiary creep (from 1 to $\sim 15\%$ strain).

The major strength of [47, 54, 74] formulations is the numerical efficiency that makes it suitable for large-scale modelling (glaciers, ice sheets), providing that transient behaviors are not of concern. In such context, the R^3iCe model could be a good candidate to provide constraints to formulate parameterizations for the temporal evolution, destined to less costly formulations.

The *CTI-RX* model is not limited to the loading conditions prescribed here or to polycrystalline ice. Its formulation is generic and can be extended to other polycrystalline materials, provided that their single crystal viscoplastic behavior can be adequately described using the Continuous Transverse Isotropic (CTI) law as defined in equation (13). For instance, the versatility of the *CTI-RX* model could enable analyzing the mechanical behavior of materials such as e.g. magnesium and quartz, which also show a strong viscoplastic anisotropy with hexagonal symmetry.

7. Conclusions

In this paper, we present a new formulation, *CTI-RX*, to model the effect of dynamic recrystallization on the texture evolution of polycrystalline materials, provided their viscoplastic behavior can be described using a Continuous Transverse Isotropic law. It is validated in the context of polycrystalline ice.

The integration of an orientation attractor, denoted as \mathbf{c}_0 along with an anisotropic flow law in a full-field resolution, allows for the accurate replication of texture evolution during dynamic recrystallization in tertiary creep under various stress conditions. This is made possible by defining \mathbf{c}_0 such as to maximize the local resolved shear stress, and therefore providing a

physically-based formulation of recrystallization-induced **c**-axes rotation. This formulation is as simple as possible, given our knowledge of the mechanisms involved.

The $R^3 iCe$ model is the result of the implementation of the *CTI-RX* formulation in a Finite Element framework. In the model, the texture results from a balance between **c**-axis rotation due to viscoplastic deformation and to dynamic recrystallization, which is controlled by Γ_{RX} , the only tuning parameter of the model. The $R^3 iCe$ model can therefore be used to constrain the impact of experimental conditions, such as pressure and temperature, on the recrystallization kinetics.

The accurate reproduction of the textures in the $R^3 iCe$ model leads to a good prediction of the mechanical softening associated with dynamic recrystallization. It confirms that texture-induced viscoplastic anisotropy may explain most of the mechanical softening observed during tertiary creep and suggests that recovery and grain boundary migration play a secondary role in this softening.

In conditions of high stresses, where confining pressure is request in the laboratory to prevent failure, we show that the expected local fracturing at the crystal scale likely enhances dynamic recrystallization processes and fasten texture evolution with strain. This is revealed by the lower Γ_{RX} required to fit the texture measured during the confined compression experiments [30] relative to that used to fit the low stress unconfined compression creep experiments [28], despite the higher experimental temperature of the latter ($-5^\circ C$ vs. $-10^\circ C$, cf. table 3). It is an additional illustration of the ability of the $R^3 iCe$ model to help resolve open questions about ice deformation behavior.

The computational cost of the $R^3 iCe$ full-field model is not adapted to a direct implementation in large-scale flow modeling frameworks. The model is nonetheless highly valuable to constrain the parameterization required to properly account for the texture evolution and its impact on the mechanical response in complex or changing boundary conditions as those prevailing in the bottom of deep ice cores, ice streams, and glaciers.

Conflicts of interest

The authors declare that the research was conducted in the absence of any commercial or financial relationships that could be construed as a potential conflict of interest.

Funding

This work was supported by the European Research Council (ERC) under the European Union's Horizon 2020 Research and Innovation programme [grant agreement No 882450 – ERC RhEoVOLUTION]

Kevin Fourteau have received funding from the European Research Council (ERC) under the European Union's Horizon 2020 research and innovation program (IVORI, grant no. 949516).

Acknowledgements

The author are thankful to Chao Qi to quickly providing the EBSD data from [30] to test $R^3 iCe$ abilities during deformation under confining pressure and high stresses.

All the computations presented in this paper were performed using the GRICAD infrastructure (<https://gricad.univ-grenoble-alpes.fr>), which is supported by Grenoble research communities.

Authors' contributions

Thomas Chauve carried out most of the study, developed the model, performed the numerical implementation of R^3iCe , the simulations, their analyses and interpretations and drafted the manuscript.

Maurine Montagnat elaborated the scientific question, participated in the development of the equations and followed the whole implementation of the model. She participated to the analyses and interpretation of the results. She is co-principal author of the paper with TC.

Véronique Dansereau participated to the elaboration of the scientific question and co-developed the model with TC. She participated to the writing of the manuscript.

Pierre Saramito helped with the development of the model from theoretical aspect to technical solution.

Kevin Fourteau proposed with TC and MM the use of an attractor to model dynamic recrystallization.

Andréa Tommasi obtained the funding and contributed to the evaluation of the model and to the writing of the final versions of the manuscript.

All authors read and approved the final manuscript.

Open Access

This article is licensed under a Creative Commons Attribution 4.0 International License, which permits use, sharing, adaptation, distribution and reproduction in any medium or format, as long as you give appropriate credit to the original author(s) and the source, provide a link to the Creative Commons license, and indicate if changes were made. The images or other third party material in this article are included in the article's Creative Commons license, unless indicated otherwise in a credit line to the material. If material is not included in the article's Creative Commons license and your intended use is not permitted by statutory regulation or exceeds the permitted use, you will need to obtain permission directly from the copyright holder. To view a full copy of this license, visit <http://creativecommons.org/licenses/by/4.0/>.

The R^3iCe code is available under GPL-v3 licence. Gitlab repository https://gricad-gitlab.univ-grenoble-alpes.fr/mecaiceige/tools/ice-polycrystal-models/rheolef_cti. The associated documentation is available at https://mecaiceige.gricad-pages.univ-grenoble-alpes.fr/tools/ice-polycrystal-models/ipms_documentation/Intro.html

Appendix A. Demonstration of δ_i identification

A.1. Constitutive equation CTI and single crystal behavior

The constitutive equation is:

$$\mathbf{D} = \left(\frac{\partial \phi_s^{(1)}}{\partial \mathbf{S}} \right)^D = 2\delta_1 \mathbf{S} + 2\delta_2 \mathbf{M}^D \text{Tr}(\mathbf{MS}) + \delta_3 (\mathbf{MS} + \mathbf{SM})^D \quad (32)$$

The single crystal anisotropy can be described by three parameters derived for experimental data :

- ψ_1 is the fluidity for parallel shearing to the basal plane :

$$g_{D_{13}} = \frac{\psi_1}{2} g_{S_{13}}, \quad g_{D_{23}} = \frac{\psi_1}{2} g_{S_{23}}$$

- β is the viscosity ratio between shear parallel to the basal plane η and the viscosity for shear within the basal plane :

$${}^g D_{12} = \beta \frac{\psi_1}{2} {}^g S_{12}$$

- γ is the viscosity ratio between compression (or traction) along the c axis η_c and compression (or traction) in one direction ${}^g e_r$ within the basal plane:

$${}^g S_{33} = 2\eta_c {}^g D_{33}, \quad \gamma {}^g S_{rr} = 2\eta_c {}^g D_{rr}$$

The same compressive (or extensive) stress parallel and normal to the \mathbf{c} -axis $S = {}^g S_{33} = {}^g S_{rr}$ results therefore in different strain rates:

$${}^g D_{rr} = \gamma {}^g D_{33}$$

A.2. δ_i identification

To identify the parameters $(\delta_1, \delta_2, \delta_3)$ in the constitutive equation (32), we developed it and compared to the single crystal behavior.

Using $\mathbf{c} = (0, 0, 1)$

$$\mathbf{M} = \begin{bmatrix} 0 & 0 & 0 \\ 0 & 0 & 0 \\ 0 & 0 & 1 \end{bmatrix}, \quad \mathbf{M}^D = \frac{1}{3} \begin{bmatrix} -1 & 0 & 0 \\ 0 & -1 & 0 \\ 0 & 0 & 2 \end{bmatrix}, \quad Tr(\mathbf{M}^g \mathbf{D}) = {}^g D_{33}$$

$$(1) \quad \delta_1 \text{ is given by applying a stress } {}^g \mathbf{S} = \begin{bmatrix} 0 & {}^g S_{12} & 0 \\ {}^g S_{12} & 0 & 0 \\ 0 & 0 & 0 \end{bmatrix}$$

Then

$$Tr(\mathbf{M}\mathbf{S}) = 0, \quad (\mathbf{M}\mathbf{S} + \mathbf{S}\mathbf{M})^D = 0$$

The constitutive equation gives :

$${}^g D_{12} = 2\delta_1 {}^g S_{12}$$

Therefore :

$$\delta_1 = \frac{\psi_1 \beta}{4}$$

$$(2) \quad \delta_3 \text{ is given by applying a stress } {}^g \mathbf{S} = \begin{bmatrix} 0 & 0 & {}^g S_{13} \\ 0 & 0 & 0 \\ {}^g S_{13} & 0 & 0 \end{bmatrix} :$$

Then

$$Tr(\mathbf{M}\mathbf{S}) = 0, \quad (\mathbf{M}\mathbf{S} + \mathbf{S}\mathbf{M})^D = \mathbf{S}$$

The constitutive equation gives :

$${}^g D_{13} = (2\delta_1 + \delta_3) {}^g S_{13}$$

Therefore

$$\delta_3 = \frac{\psi_1}{2} (1 - \beta)$$

(3) δ_2 identification is less trivial and presented in more details.

- First, a uniaxial stress $\tilde{\sigma}$ is applied along the **c**-axis. The stress tensor is ${}^g\sigma = \begin{bmatrix} 0 & 0 & 0 \\ 0 & 0 & 0 \\ 0 & 0 & \tilde{\sigma} \end{bmatrix}$

and the associated deviatoric stress tensor is ${}^g\mathbf{S} = \begin{bmatrix} -\frac{1}{3}\tilde{\sigma} & 0 & 0 \\ 0 & -\frac{1}{3}\tilde{\sigma} & 0 \\ 0 & 0 & \frac{2}{3}\tilde{\sigma} \end{bmatrix}$

– $Tr(\mathbf{M}^g\mathbf{S}) = \frac{2\tilde{\sigma}}{3}$

– $(\mathbf{M}^g\mathbf{S} + {}^g\mathbf{S}\mathbf{M})^D = \begin{bmatrix} 0 & 0 & 0 \\ 0 & 0 & 0 \\ 0 & 0 & \frac{4}{3}\tilde{\sigma} \end{bmatrix}^D = \begin{bmatrix} -\frac{4}{9}\tilde{\sigma} & 0 & 0 \\ 0 & -\frac{4}{9}\tilde{\sigma} & 0 \\ 0 & 0 & \frac{8}{9}\tilde{\sigma} \end{bmatrix}$

- using the constitutive equation, we obtain for ${}^gD_{33}$:

$${}^gD_{33} = \delta_1 \frac{4}{3}\tilde{\sigma} + \delta_2 \frac{8}{9}\tilde{\sigma} + \delta_3 \frac{8}{9}\tilde{\sigma}$$

- Then a uniaxial stress $\tilde{\sigma}$ is applied normal to the **c**-axis, for instance in the direction

1. The stress tensor is ${}^g\sigma = \begin{bmatrix} \tilde{\sigma} & 0 & 0 \\ 0 & 0 & 0 \\ 0 & 0 & 0 \end{bmatrix}$ and the associated deviatoric stress tensor is

$${}^g\mathbf{S} = \begin{bmatrix} \frac{2}{3}\tilde{\sigma} & 0 & 0 \\ 0 & -\frac{1}{3}\tilde{\sigma} & 0 \\ 0 & 0 & -\frac{1}{3}\tilde{\sigma} \end{bmatrix}$$

– $Tr(\mathbf{M}^g\mathbf{S}) = -\frac{\tilde{\sigma}}{3}$

– $(\mathbf{M}^g\mathbf{S} + {}^g\mathbf{S}\mathbf{M})^D = \begin{bmatrix} 0 & 0 & 0 \\ 0 & 0 & 0 \\ 0 & 0 & -\frac{2}{3}\tilde{\sigma} \end{bmatrix}^D = \begin{bmatrix} \frac{2}{9}\tilde{\sigma} & 0 & 0 \\ 0 & \frac{2}{9}\tilde{\sigma} & 0 \\ 0 & 0 & \frac{4}{9}\tilde{\sigma} \end{bmatrix}$

- using the constitutive equation, we obtain for ${}^gD_{11}$:

$${}^gD_{11} = \delta_1 \frac{4}{3}\tilde{\sigma} + \delta_2 \frac{2}{9}\tilde{\sigma} + \delta_3 \frac{2}{9}\tilde{\sigma}$$

- Finally from the grain behavior we can write that $\gamma {}^gD_{33} = {}^gD_{11}$:

$$\gamma \left(\frac{4}{3}\delta_1 + \frac{8}{9}\delta_2 + \frac{8}{9}\delta_3 \right) = \frac{4}{3}\delta_1 + \frac{2}{9}\delta_2 + \frac{2}{9}\delta_3$$

- This gives :

$$\delta_2 = 6\delta_1 \frac{1-\gamma}{4\gamma-1} - \delta_3$$

- and using δ_1 and δ_3 as defined above:

$$\delta_2 = \frac{\psi_1}{2} \left(\beta \frac{\gamma+2}{4\gamma-1} - 1 \right)$$

Appendix B. Strain and stress field comparison

The figures 12 and 13 show the probability distribution functions for all components of the strain and stress tensors during uniaxial creep with **c**-axis evolution (section 4.1).

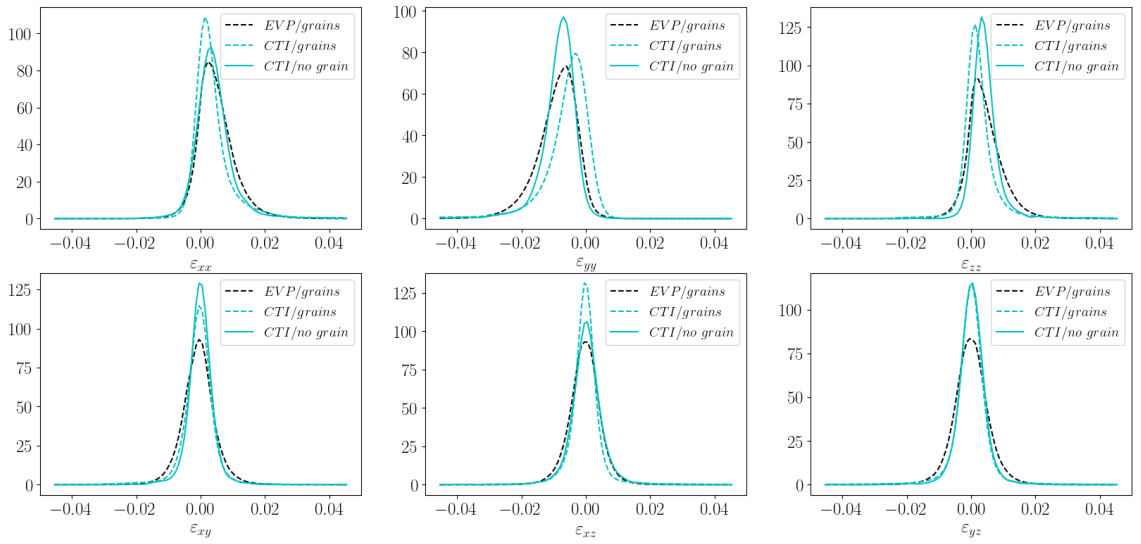


Figure 12. Kernel Density Estimation of all components of the strain tensor predicted by an elasto-viscoplastic (EVP) simulation using CraFT and the Continuous Transverse Isotropic (CTI) using $R^3 iCe$ after 0.01 macroscopic strain. The dashed lines show results for simulations where grains are well discretized. The full line show results for the simulation where a different orientation is attributed to each element.

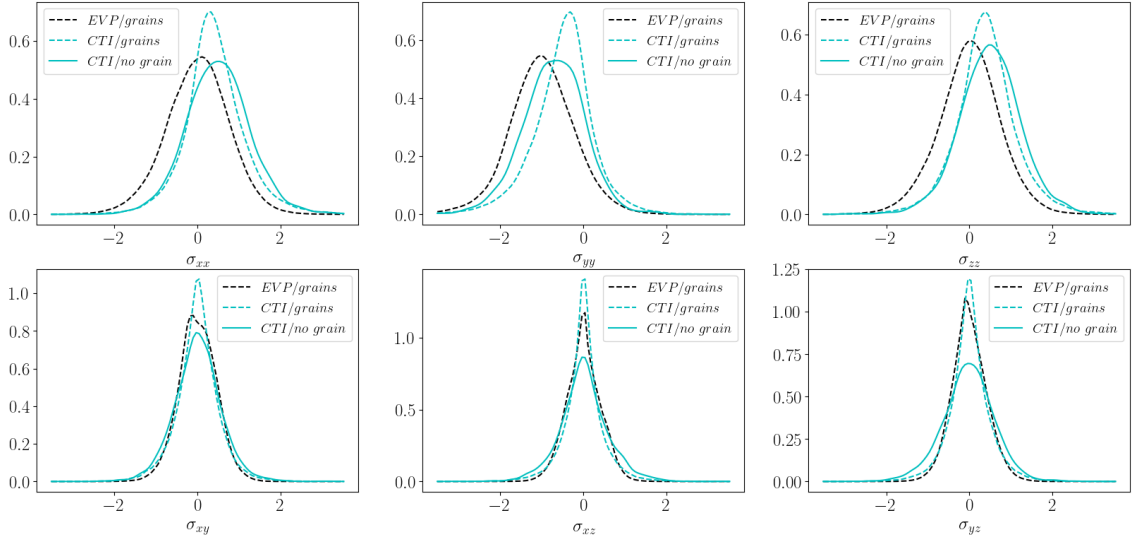


Figure 13. Kernel Density Estimation of all components of the stress tensor predicted by an elasto-viscoplastic (EVP) simulation using CraFT and the Continuous Transverse Isotropic (CTI) using $R^3 iCe$ after 0.01 macroscopic strain. The dashed lines show results for simulations where grains are well discretized. The full line show results for the simulation where a different orientation is attributed to each element.

References

- [1] F. J. Humphreys, M. Hatherly, *Recrystallization and related annealing phenomena*, Second ed., Pergamon, Oxford, 2004.
- [2] B. Kamb, "Experimental recrystallization of ice under stress" (H. C. Heard, I. Y. Borg, N. L. Carter, C. B. Raleigh, eds.), vol. 16, American Geophysical Union, 1972, p. 211-241.
- [3] J.-P. Poirier, *Creep of crystals*, Cambridge Univ. Press, 1985.
- [4] F. J. Humphreys, M. Hatherly, *Recrystallization and related annealing phenomena*, Pergamon, Oxford, 1996.
- [5] R. D. Doherty, D. A. Hughes, F. J. Humphreys, J. J. Jonas, D. J. Jensen, M. E. Kassner, W. E. King, T. R. McNelley, H. J. McQueen, A. D. Rollett, "Current issues in recrystallization: a review", *Materials Science and Engineering: A* **238** (1997), no. 2, p. 219-274.
- [6] T. Sakai, A. Belyakov, R. Kaibyshev, H. Miura, J. J. Jonas, "Dynamic and post-dynamic recrystallization under hot, cold and severe plastic deformation conditions", *Progress in Materials Science* **60** (2014), no. 0, p. 130-207.
- [7] J. W. Glen, M. F. Perutz, "The Growth and Deformation of Ice Crystals", *Journal of Glaciology* **2** (1954), no. 16, p. 397-403.
- [8] P. Duval, M. Ashby, I. Anderman, "Rate controlling processes in the creep of polycrystalline ice", *J. Phys. Chem.* **87** (1983), no. 21, p. 4066-4074.
- [9] O. Castelnau, H. Shoji, A. Mangeney, H. Milsch, P. Duval, A. Miyamoto, K. Kawada, O. Watanabe, "Anisotropic behavior of GRIP ices and flow in Central Greenland", *Earth and Planetary Science Letters* **154** (1998), no. 1-4, p. 307-322.
- [10] S. De la Chapelle, O. Castelnau, V. Lipenkov, P. Duval, "Dynamic recrystallization and texture development in ice as revealed by the study of deep ice cores in Antarctica and Greenland", *J. Geophys. Res.* **103** (1998), no. B3, p. 5091-5105.
- [11] T. Thorsteinsson, J. Kipfstuhl, H. Miller, "Textures and fabrics in the GRIP ice core", *J. Geophys. Res.* **102** (1997), no. C12, p. 26,583-26,600.
- [12] M. Montagnat, D. Buiron, L. Arnaud, A. Broquet, P. Schlitz, R. Jacob, S. Kipfstuhl, "Measurements and numerical simulation of fabric evolution along the Talos Dome ice core, Antarctica", *Earth and Planetary Science Letters* **357-358** (2012), no. 0, p. 168-178.
- [13] D. Samyn, A. Svensson, S. J. Fitzsimons, "Dynamic implications of discontinuous recrystallization in cold basal ice: Taylor Glacier, Antarctica", *Journal of Geophysical Research: Earth Surface* **113** (2008), no. F3, p. F03S90.
- [14] E. C. Smith, A. F. Baird, J. M. Kendall, C. Martín, R. S. White, A. M. Brisbourne, A. M. Smith, "Ice fabric in an Antarctic ice stream interpreted from seismic anisotropy", *Geophysical Research Letters* **44** (2017), no. 8, p. 3710-3718.
- [15] B. M. Minchew, C. R. Meyer, A. A. Robel, G. H. Gudmundsson, M. Simons, "Processes controlling the downstream evolution of ice rheology in glacier shear margins: case study on Rutford Ice Stream, West Antarctica", *Journal of Glaciology* **64** (2018), no. 246, p. 583-594.
- [16] R. E. Thomas, M. Negrini, D. J. Prior, R. Mulvaney, H. Still, M. H. Bowman, L. Craw, S. Fan, B. Hubbard, C. Hulbe, D. Kim, F. Lutz, "Microstructure and Crystallographic Preferred Orientations of an Azimuthally Oriented Ice Core from a Lateral Shear Margin: Priestley Glacier, Antarctica", *Frontiers in Earth Science* **9** (2021), p. 702213.
- [17] E. C. Pettit, T. Thorsteinsson, P. Jacobson, E. D. Waddington, "The role of crystal fabric in flow near an ice divide", *J. Glaciol.* **53** (2007), no. 181, p. 277-288.
- [18] F. Gillet-Chaulet, "Modélisation de l'écoulement de la glace polaire anisotrope et premières applications au forage de Dôme C.", PhD Thesis, Thèse de Doctorat de l'Université Joseph Fourier-Grenoble I, 2006.
- [19] C. Martín, G. H. Gudmundsson, H. D. Pritchard, O. Gagliardini, "On the effects of anisotropic rheology on ice flow, internal structure, and the age-depth relationship at ice divides", *Journal of Geophysical Research: Earth Surface* **114** (2009), no. F4.
- [20] Y. Ma, O. Gagliardini, C. Ritz, F. Gillet-Chaulet, G. Durand, M. Montagnat, "Enhancement factors for grounded ice and ice shelves inferred from an anisotropic ice-flow model", *Journal of Glaciology* **56** (2010), no. 199, p. 805-812.
- [21] W. F. Budd, R. C. Warner, T. H. Jacka, J. Li, A. Treverrow, "Ice flow relations for stress and strain-rate components from combined shear and compression laboratory experiments", *Journal of Glaciology* **59** (2013), no. 214, p. 374-392.
- [22] F. S. McCormack, R. C. Warner, H. Seroussi, C. F. Dow, J. L. Roberts, A. Treverrow, "Modeling the Deformation Regime of Thwaites Glacier, West Antarctica, Using a Simple Flow Relation for Ice Anisotropy (ESTAR)", *Journal of Geophysical Research: Earth Surface* **127** (2022), no. 3, p. e2021JF006332.
- [23] P. Duval, "Creep and recrystallization of polycrystalline ice", *Bull. Mineral* **102** (1979), p. 80-85.
- [24] P. Duval, "Creep and Fabrics of Polycrystalline Ice Under Shear and Compression", *Journal of Glaciology* **27** (1981), no. 95, p. 129-140.
- [25] J. L. Bouchez, P. Duval, "The fabric of polycrystalline ice deformed in simple shear : experiments in torsion, natural deformation and geometrical interpretation.", *Textures and microstructures* **5** (1982), p. 171-190.
- [26] T. H. Jacka, M. Maccagnan, "Ice crystallographic and strain rate changes with strain in compression and extension", *Cold Reg. Sci. Technol.* **8** (1984), p. 269-286.
- [27] T. H. Jacka, L. Jun, "The steady-state crystal size of deforming ice", *Ann. Glaciol.* **20** (1994), p. 13-18.

- [28] M. Montagnat, T. Chauve, F. Barou, A. Tommasi, B. Beausir, C. Fressengeas, "Analysis of dynamic recrystallization of ice from EBSD orientation mapping", *Frontiers in Earth Science* **3** (2015), no. 81, p. 1-13.
- [29] T. Chauve, M. Montagnat, P. Vacher, "Strain field evolution during dynamic recrystallization nucleation; A case study on ice", *Acta Materialia* **101** (2015), p. 116-124.
- [30] C. Qi, D. L. Goldsby, D. J. Prior, "The down-stress transition from cluster to cone fabrics in experimentally deformed ice", *Earth and Planetary Science Letters* **471** (2017), p. 136-147.
- [31] B. Journaux, T. Chauve, M. Montagnat, A. Tommasi, F. Barou, D. Mainprice, L. Gest, "Recrystallization processes, microstructure and crystallographic preferred orientation evolution in polycrystalline ice during high-temperature simple shear", *The Cryosphere* **13** (2019), no. 5, p. 1495-1511.
- [32] F. Grennerat, M. Montagnat, O. Castelnau, P. Vacher, H. Moulinec, P. Suquet, P. Duval, "Experimental characterization of the intragranular strain field in columnar ice during transient creep", *Acta Materialia* **60** (2012), no. 8, p. 3655-3666.
- [33] T. Chauve, M. Montagnat, F. Barou, K. Hidas, A. Tommasi, D. Mainprice, "Investigation of nucleation processes during dynamic recrystallization of ice using cryo-EBSD", *Philosophical Transactions of the Royal Society A: Mathematical, Physical and Engineering Sciences* **375** (2017), no. 2086, p. 20150345.
- [34] T. Jacka, W. Budd, "The use of tertiary creep rates in ice at high strains in compression and shear", in *Ice-Structure Interaction: IUTAM/IAHR Symposium St. John's, Newfoundland Canada 1989*, Springer, 1991, p. 21-35.
- [35] L. Jun, T. H. Jacka, "Horizontal shear rate of ice initially exhibiting vertical compression fabrics", *Journal of Glaciology* **44** (1998), no. 148, p. 670-672.
- [36] J. Li, T. Jacka, W. Budd, "Deformation rates in combined compression and shear for ice which is initially isotropic and after the development of strong anisotropy", *Annals of Glaciology* **23** (1996), no. 1, p. 247-252.
- [37] A. Treverrow, W. F. Budd, T. H. Jacka, R. C. Warner, "The tertiary creep of polycrystalline ice: experimental evidence for stress-dependent levels of strain-rate enhancement", *Journal of Glaciology* **58** (2012), no. 208, p. 301-314.
- [38] J. W. Glen, "Experiments on the Deformation of Ice", *Journal of Glaciology* **2** (1952), no. 12, p. 111-114.
- [39] S. Piazzolo, C. J. L. Wilson, V. Luzin, C. Brouzet, M. Peternell, "Dynamics of ice mass deformation: Linking processes to rheology, texture, and microstructure", *Geochemistry, Geophysics, Geosystems* **14** (2013), no. 10, p. 4185-4194.
- [40] P. J. Hudleston, "Progressive development of fabrics across zones of shear in glacial ice" (S. K. Saxena, S. Bhattacharji, eds.), Springer-Verlag, New York, 1977, p. 121-150.
- [41] C. Qi, D. J. Prior, L. Craw, S. Fan, M. G. Llorens, A. Griera, M. Negrini, P. D. Bons, D. L. Goldsby, "Crystallographic preferred orientations of ice deformed in direct-shear experiments at low temperatures", *The Cryosphere* **13** (2019), no. 1, p. 351-371.
- [42] R. B. Alley, "Fabrics in polar ice sheets - Development and prediction", *Science* **240** (1988), p. 493-495.
- [43] O. Castelnau, T. Thorsteinsson, J. Kipfstuhl, P. Duval, G. R. Canova, "Modelling fabric development along the GRIP ice core, central Greenland", *Ann. Glaciol.* **23** (1996), p. 194-201.
- [44] H. R. Wenk, G. Canova, Y. Bréchet, L. Flandin, "A deformation-based model for recrystallization of anisotropic materials", *Acta. Mater.* **45** (1997), no. 8, p. 3283-3296.
- [45] T. Thorsteinsson, "An analytical approach to deformation of anisotropic ice-crystal aggregates", *Journal of Glaciology* **47** (2001), no. 158, p. 507-516.
- [46] M.-G. Llorens, A. Griera, P. D. Bons, R. A. Lebensohn, L. A. Evans, D. Jansen, I. Weikusat, "Full-field predictions of ice dynamic recrystallisation under simple shear conditions", *Earth and Planetary Science Letters* **450** (2016), p. 233-242.
- [47] D. H. M. Richards, S. Pegler, S. Piazzolo, O. G. Harlen, "The evolution of ice fabrics: A continuum modelling approach validated against laboratory experiments", *Earth and Planetary Science Letters* **556** (2021), p. 116718.
- [48] N. M. Rathmann, C. S. Hvidberg, A. Grinsted, D. A. Lilien, D. Dahl-Jensen, "Effect of an orientation-dependent non-linear grain fluidity on bulk directional enhancement factors", *Journal of Glaciology* (2021), p. 1-7.
- [49] O. Castelnau, P. Duval, R. A. Lebensohn, G. Canova, "Viscoplastic modeling of texture development in polycrystalline ice with a self-consistent approach : Comparison with bound estimates", *J. Geophys. Res.* **101** (1996), no. 6, p. 13,851-13,868.
- [50] J. Meyssonier, A. Philip, "A model for the tangent viscous behaviour of anisotropic polar ice", *Annals of Glaciology* **23** (1996), p. 253-261.
- [51] P. Mansuy, J. Meyssonier, A. Philip, "Localization of deformation in polycrystalline ice: experiments and numerical simulations with a simple grain model", *Computational Materials Science* **25** (2002), no. 1-2, p. 142-150.
- [52] F. Gillet-Chaulet, O. Gagliardini, J. Meyssonier, M. Montagnat, O. Castelnau, "A user-friendly anisotropic flow law for ice-sheet modelling", *J. Glaciol.* **41** (2005), no. 172, p. 3 - 14.
- [53] A. Burr, W. Noël, P. Treccourt, M. Bourcier, F. Gillet-Chaulet, A. Philip, C. L. Martin, "The anisotropic contact response of viscoplastic monocrystalline ice particles", *Acta Materialia* **132** (2017), p. 576-585.
- [54] N. M. Rathmann, D. A. Lilien, "Inferred basal friction and mass flux affected by crystal-orientation fabrics", *Journal of Glaciology* (2021), p. 1-17.
- [55] J. P. Boehler, L. E. Aoufi, J. Raclin, "On Experimental Testing Methods for Anisotropic Materials", *Res Mech.* **21** (1987), p. 73-95.

- [56] F. Gillet-Chaulet, O. Gagliardini, J. Meyssonier, T. Zwinger, J. Ruokolainen, "Flow-induced anisotropy in polar ice and related ice-sheet flow modelling", *J. Non-Newtonian Fluid Mech.* **134** (2006), p. 33-43.
- [57] O. Gagliardini, F. Gillet-Chaulet, M. Montagnat, "A review of anisotropic polar ice models: from crystal to ice-sheet flow models" (T. Hondoh, ed.), vol. 68, Supplement Issue of Low Temperature Science, Hokkaido University, 2009, p. 149-166.
- [58] L. Lliboutry, "Anisotropic, transversely isotropic nonlinear viscosity of rock ice and rheological parameters inferred from homogenization", *Int. J. Plast.* **9** (1993), p. 619-632.
- [59] N. Azuma, "A flow law for anisotropic polycrystalline ice under uniaxial compressive deformation", *Cold Reg. Sci. Technol.* **23** (1995), p. 137-147.
- [60] B. Svendsen, K. Hutter, "A continuum approach for modelling induced anisotropy in glaciers and ice sheets", *Ann. Glaciol.* **23** (1996), p. 262-269.
- [61] G. Gödert, K. Hutter, "Induced anisotropy in large ice shields: Theory and its homogenization", *Continuum Mech. Thermodyn.* **10** (1998), p. 293-318.
- [62] H.-C. Wu, *Continuum mechanics and plasticity*, Crc Press, 2004.
- [63] P. Saramito, "Efficient C++ finite element computing with Rheolef", p. 279.
- [64] S. Piazzolo, M. Montagnat, F. Grennerat, H. Moulinec, J. Wheeler, "Effect of local stress heterogeneities on dislocation fields: Examples from transient creep in polycrystalline ice", *Acta Materialia* **90** (2015), no. 0, p. 303-309.
- [65] P. Suquet, H. Moulinec, O. Castelnau, M. Montagnat, N. Lahellec, F. Grennerat, P. Duval, R. Brenner, "Multi-scale modeling of the mechanical behavior of polycrystalline ice under transient creep", *Procedia IUTAM* **3** (2012), p. 76-90.
- [66] R. Quey, P. Dawson, F. Barbe, "Large-scale 3D random polycrystals for the finite element method: Generation, meshing and remeshing", *Computer Methods in Applied Mechanics and Engineering* **200** (2011), no. 17, p. 1729-1745.
- [67] O. Castelnau, G. R. Canova, R. A. Lebensohn, P. Duval, "Modelling viscoplastic behavior of anisotropic polycrystalline ice with a self-Consistent approach", *Acta Materialia* **45** (1997), no. 11, p. 4823-4834.
- [68] T. H. Jacka, "The time and strain required for development of minimum strain rates in ice", *Cold Reg. Sci. Technol.* **3** (1984), p. 261-268.
- [69] J. P. Burg, C. J. L. Wilson, J. C. Mitchell, "Dynamic recrystallization and fabric development during the simple shear deformation of ice", *Journal of Structural Geology* **8** (1986), no. 8, p. 857-870.
- [70] M. Mellor, D. M. Cole, "Deformation and failure of ice under constant stress or constant strain-rate", *Cold Regions Science and Technology* **5** (1982), no. 3, p. 201-219.
- [71] T. Chauve, M. Montagnat, S. Piazzolo, B. Journaux, J. Wheeler, F. Barou, D. Mainprice, A. Tommasi, "Non-basal dislocations should be accounted for in simulating ice mass flow", *Earth and Planetary Science Letters* **473** (2017), p. 247-255.
- [72] T. Chauve, M. Montagnat, C. Lachaud, D. Georges, P. Vacher, "Strain field evolution at the ductile-to-brittle transition: a case study on ice", *Solid Earth* **8** (2017), no. 5, p. 943-953.
- [73] P. Kalifa, G. Ouillon, P. Duval, "Microcracking and the failure of polycrystalline ice under triaxial compression", *Journal of Glaciology* **38** (1992), no. 128, p. 65-76.
- [74] D. H. Richards, S. Pegler, S. Piazzolo, "Ice fabrics in two-dimensional flows: beyond pure and simple shear", *The Cryosphere* **16** (2022), no. 10, p. 4571-4592.